REPORT DOCUMENTATION PAGE

Form Approved
OMB NO. 0704-0188

Public Reporting burden for this collection of information is estimated to average 1 hour per response, including the time for reviewing instructions, searching existing data sources, gathering and maintaining the data needed, and completing and reviewing the collection of information. Send comment regarding this burden estimates or any other aspect of this collection of information, including suggestions for reducing this burden, to Washington Headquarters Services, Directorate for information Operations and Reports, 1215 Jefferson Davis Highway, Suite 1204, Arlington, VA 22202-4302, and to the Office of Management and Budget, Paperwork Reduction Project (0704-0188,) Washington, DC 20503.

1. AGENCY USE ONLY (Leave Blank)	2. REPORT DATE 31 May 2007	3. REPORT TYPE AND DATES COVERED 01 August, 06 – 30 April 07

4. TITLE AND SUBTITLE

Hearing Protection for High-Noise Environments

5. FUNDING NUMBERS
FA9550-06-C-0034

6. AUTHOR(S)
Elizabeth Bleszynski, Marek Bleszynski, Thomas Jaroszewicz

7. PERFORMING ORGANIZATION NAME(S) AND ADDRESS(ES)
Monopole Research
739 Calle Sequoia, Thousand Oaks, CA 91360

8. PERFORMING ORGANIZATION REPORT NUMBER
MON0003

9. SPONSORING / MONITORING AGENCY NAME(S) AND ADDRESS(ES)

Air Force Office of Scientific Research
875 North Randolph Rd., Room 3112
Arlington, VA 22203
Dr Willard Larkin/NL

10. SPONSORING / MONITORING AGENCY REPORT NUMBER

11. SUPPLEMENTARY NOTES
The views, opinions and/or findings contained in this report are those of the author(s) and should not be construed as an official Department of the Air Force position, policy or decision, unless so designated by other documentation.

12 a. DISTRIBUTION / AVAILABILITY STATEMENT

Approved for public release, distribution unlimited.

12 b. DISTRIBUTION CODE

AFRL-SR-AR-TR-07-0331

13. ABSTRACT (Maximum 200 words)

Report developed under STTR contract for topic AF06-T035.

The objective of our effort was to develop powerful software tools and to perform high fidelity simulation which would allow identification and understanding of relevant bioacoustic and psychoacoustic mechanisms responsible for the transmission of acoustic energy through non-airborne pathways to the cochlea.

As the main achievements of our Phase I work we consider:

- development of a set of algorithms (including non-lossy, error-controlled matrix compression techniques) for general, i.e., variable-density, volumetric equations of acoustics, and

- development of a solution technique overcoming ill-conditioning difficulties arising in large density contrast problems.

14. SUBJECT TERMS			15. NUMBER OF PAGES part I : V + 53 part II: III + 43
STTR report, bone conducted sound, computational acoustics, integral equations, FFT–based matrix compression			
			16. PRICE CODE

17. SECURITY CLASSIFICATION OR REPORT **UNCLASSIFIED**	18. SECURITY CLASSIFICATION ON THIS PAGE **UNCLASSIFIED**	19. SECURITY CLASSIFICATION OF ABSTRACT **UNCLASSIFIED**	20. LIMITATION OF ABSTRACT **UL**

NSN 7540-01-280-5500

Standard Form 298 (Rev.2-89)
Prescribed by ANSI Std. 239-18
298-102

Phase I Final Report, Part I

HEARING PROTECTION FOR HIGH-NOISE ENVIRONMENTS

Contract # **FA9550-06-C-0034**

Topic # **AF06-T035**

Period of Performance: **August 01, 2006 - April 30, 2007**

Prepared by:

MONOPOLE RESEARCH
739 Calle Sequoia, Thousand Oaks, CA 91360
tel: **(805) 375-0318**   fax: **(805) 499-9878**

Distribution unlimited

20070910353

Contents

List of Figures

iv

List of Tables

1 Executive summary

In the light of

- the seriousness of the noise-induced hearing damage,

- the lack of fundamental knowledge regarding transmission of acoustic energy through non-airborne pathways to the cochlea, and,

- difficulties associated with designing experiments reproducing realistic conditions of sound propagation through the human head,

our objective has been to develop rigorous algorithms and to construct corresponding efficient software tools allowing high fidelity numerical simulations of sound wave propagation through biological tissues.

As the main achievements of our Phase I work we consider:

- development of a set of algorithms (including ***non-lossy, error-controlled matrix compression techniques***) for general, i.e., ***variable-density***, volumetric equations of acoustics; and

- development of a solution technique overcoming ill-conditioning difficulties arising in ***large density contrast problems.***

We believe that, in this way, we contributed a practically useful and efficient approach for solving a large class of problems of acoustic wave propagation through inhomogeneous media, including propagation of sound through the human body.

To execute the proposed effort, we combined capabilities and expertise in the areas of :

- development of fast solvers for realistic, parallel, large scale simulations (Monopole Research),

- generation of accurate geometry representations (UT Austin) and,

- identification and execution of relevant acoustic wave experiments (UT Austin).

1

2 Objective and brief approach description

To reiterate, the objective of our effort was

to develop powerful software tools and to perform high fidelity simulations which would allow identification and understanding of relevant bioacoustic and psychoacoustic mechanisms responsible for the transmission of acoustic energy through non-airborne pathways to the cochlea.

As our tool for simulating sound propagation in the human body, we chose an approach based on volumetric integral equations. The well known advantages of the integral-equation formulation include its high numerical accuracy, stability, and exact treatment of the boundary conditions at infinity (and, hence, no need of discretizing any regions of the space surrounding the scatterer).

The main reason why integral equations had not been more commonly used in acoustics is their high computational cost: a straightforward integral-equation discretization leads to the costs of at least $O(N^2)$ for iterative and $O(N^3)$ for the direct solution methods. However, adaptation of presently available **matrix compression** and **fast solution techniques** [1, 2] to acoustics, as described in Section 3.3, reduces that cost to approximately $O(N)$, and thus renders large integral-equation problems tractable.

Another issue arising in applying the integral-equation formulation to sound scattering on a body surrounded by air is the necessity of taking into account the **spatial variability of the medium density**, as the ratio of a biological tissue density to that of air is about 1000. Our development of a **two-stage solution technique** constitutes, to our knowledge, the first practical numerical implementation which overcomes ill-conditioning caused by large density contrasts, and results in a well-posed problem. [1]

In what follows we briefly describe the main results and accomplishments of our Phase I work.

3 Summary of Phase I results

3.1 Formulation and implementation of an integral-equation approach in acoustics

We present here the motivation of our choice of the integral equations as the mathematical modeling tool, and give a short description of our integral

---

[1]We note that much of the existing work on "acoustics integral equations" has been concerned exclusively with *constant-density* problems.

equations and their discretization. Further technical details are given in Appendices A and B.

Volumetric integral equations. Volumetric integral equations for the pressure field – known generally as the Lippmann-Schwinger (L-S) equations – can be derived from the differential equation of acoustics split into two terms: one describing wave propagation in the background medium (in our case, air) and the other wave interaction with the scatterer (here, the human head), occupying the spatial region Ω.

The resulting L-S equation [3] for the pressure field $p(\mathbf{r})$ is

$$
p^{(\text{inc})}(\mathbf{r}) = p(\mathbf{r}) + \int_{\Omega} \mathrm{d}^3 r' \left\{ k^2 \, g(\mathbf{r} - \mathbf{r}') \left(1 - \frac{\kappa(\mathbf{r}')}{\kappa_0} \right) p(\mathbf{r}') \right.
$$

$$
\left. - \left[\nabla_{\mathbf{r}'} \, g(\mathbf{r} - \mathbf{r}') \right] \cdot \left(1 - \frac{\rho_0}{\rho(\mathbf{r}')} \right) \nabla_{\mathbf{r}'} \, p(\mathbf{r}') \right\} , \tag{3.1}
$$

where $p^{(\text{inc})}$ is the incident wave, satisfying the Helmholtz equation in the background medium, and g is the corresponding Green function,

$$
g(\mathbf{r}) = \frac{e^{i\,k\,|\mathbf{r}|}}{4\pi|\mathbf{r}|} . \tag{3.2}
$$

The details of the derivation are given in Appendix A.

Discretization of the volumetric integral equations. In the Galerkin discretization scheme we expand the pressure in terms of a set of scalar locally supported trial basis functions ϕ_α,

$$
p(\mathbf{r}) = \sum_{\alpha=1}^{N} x_\alpha \, \phi_\alpha(\mathbf{r}) , \tag{3.3}
$$

and use the same set as testing functions.

The details of the derivation are described in Appendix B. Here we give the final result:

The discretized equation (3.1) becomes the matrix equation

$$
\sum_{\beta=1}^{N} A_{\alpha\beta} \, x_\beta = b_\alpha , \qquad \text{for } \alpha = 1, 2, \cdots, N , \tag{3.4}
$$

3

where the r.h.s.
$$b_\alpha = \int d^3r \, \phi_\alpha(\mathbf{r}) \, p^{(\text{inc})}(\mathbf{r}) \tag{3.5}$$

represents the incident pressure field, and the elements of the matrix A are

$$A_{\alpha\beta} = \int d^3r \, \phi_\alpha(\mathbf{r}) \, \phi_\beta(\mathbf{r}) \tag{3.6a}$$

$$- k^2 \int d^3r_1 \, d^3r_2 \, \phi_\alpha(\mathbf{r}_1) \, g(\mathbf{r}_1 - \mathbf{r}_2) \left(1 - \frac{\kappa(\mathbf{r}_2)}{\kappa_0} \right) \phi_\beta(\mathbf{r}_2) \tag{3.6b}$$

$$- \int d^3r_1 \, d^3r_2 \, \left[\nabla_{\mathbf{r}_1} \phi_\alpha(\mathbf{r}_1) \right] g(\mathbf{r}_1 - \mathbf{r}_2) \cdot \left(1 - \frac{\rho_0}{\rho(\mathbf{r}_2)} \right) \left[\nabla_{\mathbf{r}_2} \phi_\beta(\mathbf{r}_2) \right]$$
$$\tag{3.6c}$$

$$\equiv \int d^3r \, \phi_\alpha(\mathbf{r}) \frac{\rho_0}{\rho(\mathbf{r})} \phi_\beta(\mathbf{r}) \tag{3.6d}$$

$$+ k^2 \int d^3r_1 \, d^3r_2 \, \phi_\alpha(\mathbf{r}_1) \, g(\mathbf{r}_1 - \mathbf{r}_2) \left(\frac{\kappa(\mathbf{r}_2)}{\kappa_0} - \frac{\rho_0}{\rho(\mathbf{r}_2)} \right) \phi_\beta(\mathbf{r}_2) \tag{3.6e}$$

$$- \int d^3r_1 \, d^3r_2 \, \left[\nabla_{\mathbf{r}_1} \phi_\alpha(\mathbf{r}_1) \right] g(\mathbf{r}_1 - \mathbf{r}_2) \cdot \left(\nabla_{\mathbf{r}_2} \frac{\rho_0}{\rho(\mathbf{r}_2)} \right) \phi_\beta(\mathbf{r}_2) \tag{3.6f}$$

$$\equiv A^{\text{R}}_{\alpha\beta} + A^{\text{M}}_{\alpha\beta} + A^{\text{D}}_{\alpha\beta} . \tag{3.6g}$$

In the following we refer to the terms A^{R}, A^{M}, and A^{D} (given by Eqs. (3.6d) – (3.6f)) as the **material**, **monopole**, and **dipole** contributions.

The two alternative expressions given in Eq.(3.6) here are equivalent. The first one is derived directly from Eq.(3.1), and the second is obtained by integrating by parts and using the definition of the Green function g (it can also be deduced from an alternative form of the differential equation given in Appendix A). However, the individual terms in these equations have quite different properties:

1. The nearly diagonal term (3.6a) is independent of the material properties, while the term (3.6d) (denoted $A^{\text{R}}_{\alpha\beta}$ in Eq.(3.6g)) does depend on ρ_0. We recall that in our case $\rho_0/\rho \sim 10^{-3}$, hence $A^{\text{R}}_{\alpha\beta}$ is small.

2. For a large distance R between the supports of the basis functions ϕ_α and ϕ_β, both the terms (3.6b) and (3.6e) behave as $1/R$, hence they can be interpreted as due to monopole-monopole (MM) couplings. However, for materials of interest, the term (3.6e) ($A^{\text{M}}_{\alpha\beta}$) is much smaller than (3.6b) (typically, $\kappa/\kappa_0 \sim 10^{-4}$).

4

3. Depending on whether $\rho(\mathbf{r})$ is constant or variable over the support of ϕ_β, the term (3.6c) behaves at large distances as $1/R^3$ or $1/R^2$, i.e., can be interpreted as a dipole-dipole (DD) or dipole-monopole (DM) coupling. The term (3.6f) ($A_{\alpha\beta}^D$), on the other hand, is nonzero only for variable $\rho(\mathbf{r})$, and then it represents a dipole-monopole (DM) coupling. Also in this case the term (3.6f) (if nonzero) is much smaller than (3.6c).

In other words, the DD and DM couplings of the term (3.6c) are converted into MM and DM coupling of the terms (3.6d) – (3.6f). Generally speaking, the individual terms (3.6a) – (3.6c) tend to be large compared to the terms (3.6d) – (3.6f), which already incorporate substantial cancellations. Therefore, from the numerical point of view, evaluation of the terms (3.6a) – (3.6c) requires a high precision, in order to ensure sufficient accuracy after cancellation. These cancellations are already taken into account in Eqs. (3.6d) – (3.6f), hence the latter are clearly preferable.

In our present solver we implemented discretizations with piecewise constant basis functions supported on tetrahedra, and with piecewise linear basis functions associated with vertices and supported on sets of tetrahedra sharing the given vertex.

An example: application to a large-contrast problem. In our applications to acoustic wave scattering on biological objects the mass/stiffness matrix of (3.6) exhibits a particular feature: the last term, the DM component $A_{\alpha\beta}^D$ of (3.6f), becomes the dominant contribution, due to the discontinuity of the ratio $\rho_0/\rho(\mathbf{r})$ at the interface of the object and the surrounding air ($\rho_0/\rho(\mathbf{r}) = 1$ outside of the object and $\rho_0/\rho(\mathbf{r}) \sim 10^{-3}$ inside). As we discussed in the points 1 and 2 above, the remaining terms, $A_{\alpha\beta}^R$ and $A_{\alpha\beta}^M$, are small, because both ρ_0/ρ and κ/κ_0 are small.

Since the **surface** term $A_{\alpha\beta}^D$ dominates, the system of equations (3.4) is much more sensitive to the values of the solution (the pressure p) on the surface, than to its values in the interior of the object. In other words, the system is ill-conditioned, and the solution inside the object is poorly defined. This fact is illustrated by the example of a scattering on a homogeneous sphere with $\rho/\rho_0 = 10^3$ and $\kappa/\kappa_0 = 10^{-4}$, and discretized with $N = 200,000$ tetrahedra (Fig. 1), and subject to an incident pressure wave of unit amplitude and the wavelength $\lambda = 6$ m. In the computation we used our fast solver code based on the FFT compression of the stiffness matrix, described in Section 3.3 and in Appendix D.

Figure 1: Distribution of the absolute value of the pressure, $|p(\mathbf{r})|$, on a plane parallel to the incident wave vector and passing through the sphere center. Analytic solution is compared with the conventional solution of the L-S integral equations for $\rho/\rho_0 = 10^3$ and $\kappa/\kappa_0 = 10^{-4}$, and for a discretization with $N = 200,000$ tetrahedra. Note different pressure scales for the two distributions.

The comparison of Fig. 1 clearly shows that the numerical solution for the pressure inside the sphere is completely unreliable. We note that the pressure distributions in the Figure are plotted in two different scales: up to 1.5 for the analytic solution and up to 10 for the numerical solution; in fact, in the latter case the pressure exceeds at some points the value 600. By introducing small artificial "errors" in the components of the r.h.s. vector b in Eq.(3.4) we also verified that small fluctuations in b cause large and unpredictable changes in the solution x. At the same time, as we have have checked, the scattering cross-section (which is, practically, sensitive only to the pressure at the object surface) is reproduced with a near perfect accuracy. Both these facts are consistent with ill-conditioning of the discretized L-S integral equations, resulting in a poorly determined solution in the interior of the object.

3.2 Development of a novel two-stage solution method for large-contrast problems

Reformulation of the integral equation system. We have found that the ill-conditioning problem encountered for large density contrast can be remedied by reformulating, in a rigorous way, the original integral equation as a set of a surface and volume equations, both of them well conditioned.

6

The details of our formulation are described in Appendix C; here we only sketch the solution procedure:

We first write the integral equation (3.1) as

$$p^{(\text{inc})} = K\,p\,, \tag{3.7}$$

and define an operator $K^{(0)}$ as the $\rho(\mathbf{r})/\rho \to \infty$ limit of the surface operator K_{s}. By construction, this operator involves only the values of the pressure on the object surface. We denote by $p_{\text{s}}^{(0)}$ the solution of the resulting **surface equation**

$$p^{(\text{inc})}(\mathbf{r}) = \big(K^{(0)}\,p_{\text{s}}^{(0)}\big)(\mathbf{r}) \qquad \text{for } \mathbf{r} \in \partial\Omega\,. \tag{3.8}$$

We can then show (Appendix C) that, if Eq.(3.8) holds on the object surface, it also holds for all points $\mathbf{r} \in \Omega$, i.e. in the object interior.

Next, we represent the operator K as

$$K = K^{(0)} + \xi\,K^{(1)} \tag{3.9}$$

with $K^{(1)} = \xi^{-1}\,(K - K^{(0)})$ and with the parameter ξ, depending on the function $\rho(\mathbf{r})$, chosen such that the operator $K^{(1)}$ remains finite when $|\rho(\mathbf{r})| \to \infty$ (we can, e.g., take ξ as the average value of $|\rho_0/\rho|$ in the region Ω).

Correspondingly, we parameterize the full solution as

$$p = p_{\text{s}}^{(0)} + \xi\,p_{\text{s}}^{(1)} + p_{\text{v}}\,, \tag{3.10}$$

where $p_{\text{s}}^{(0)}$ is previously determined surface solution of Eq.(3.8), $p_{\text{s}}^{(1)}$ is a correction to the surface solution $p_{\text{s}}^{(0)}$, and p_{v} is the volume part of the solution, defined such that

$$K^{(0)}\,p_{\text{v}} = K_{\text{s}}\,p_{\text{v}} = 0\,. \tag{3.11}$$

By substituting Eqs. (3.9) and (3.10) into Eq.(3.7) and making use of Eqs. (3.8) and (3.11), we find the **volumetric equation**

$$\big(\big[K^{(0)} + \xi\,K^{(1)}\big]\,p_{\text{s}}^{(1)}\big)(\mathbf{r}) + \big(K^{(1)}\,p_{\text{v}}\big)(\mathbf{r}) = -\big(K^{(1)}\,p_{\text{s}}^{(0)}\big)(\mathbf{r}) \quad \text{for } \mathbf{r} \in \overline{\Omega} \tag{3.12}$$

for the unknown fields $p_{\text{s}}^{(1)}$ and p_{v}, with the r.h.s. expressed in terms of the previously determined surface problem solution $p_{\text{s}}^{(0)}$.

Finally, the entire solution procedure consists of

1. solving the **surface** problem (3.8),

2. using the solution $p_{\text{s}}^{(0)}$ to compute the r.h.s. of Eq.(3.12),

7

3. solving the **volumetric** problem (3.12) for $p_s^{(1)}$ and p_v; and

4. constructing the full solution according to Eq.(3.10).

We stress that neither of the equations (3.8) and (3.12) suffer from ill-conditioning in the limit $\rho \to \infty$ ($\xi \to 0$). At the same time, since no small-ξ approximations were made, the procedure can be used for any material density. We also emphasize that these equations are coupled in one "direction" only, i.e., the volumetric equation depends on the solution of the surface equation, but not *v.v.* Hence, our system of equations does not require any iterative procedure involving alternating solutions of the surface and volume problems.

An application to a large-contrast problem. In order to demonstrate the efficacy of our two-step solution procedure, we consider again the example discussed at the end of the previous Section, 3.1 (further examples of application of the method are given in Section 3.4). Now, by using the two-step solution scheme, we obtain a stable and accurate solution, as indicated by Fig. 2.
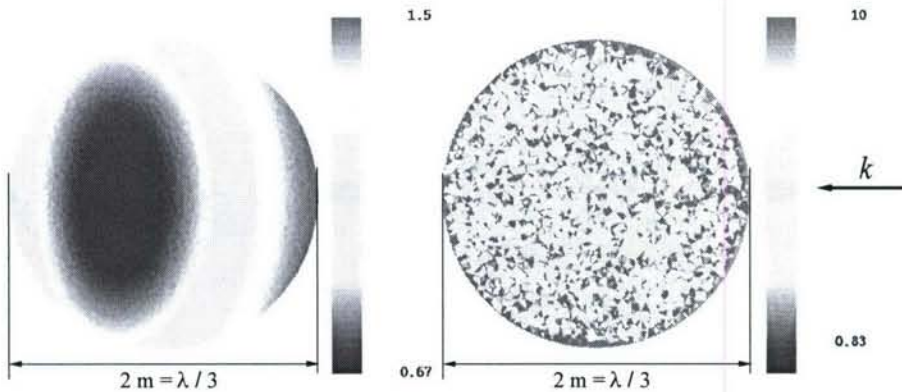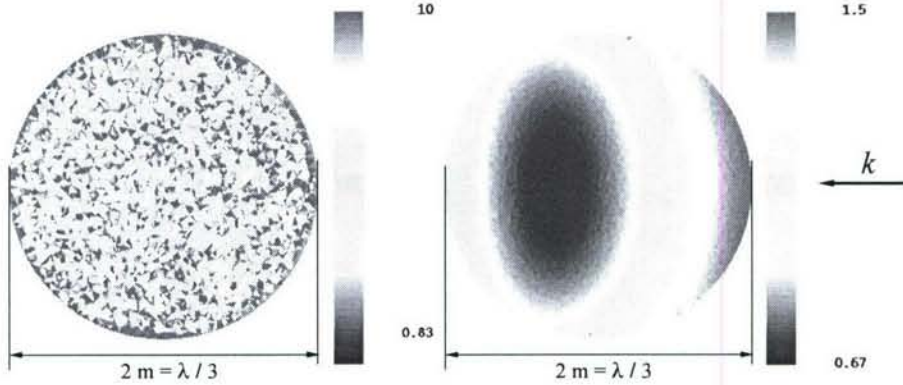

Figure 2: Distribution of the absolute value of the pressure, $|p(\mathbf{r})|$, on a plane parallel to the incident wave vector and passing through the sphere center, for the same material parameters and discretization as in Fig. 1. As before, the conventional and two-stage solutions are plotted on different scales.

The error distributions of the conventional and two-stage solutions (compared to the analytical solution) are plotted in the histograms of Fig. 3.

8
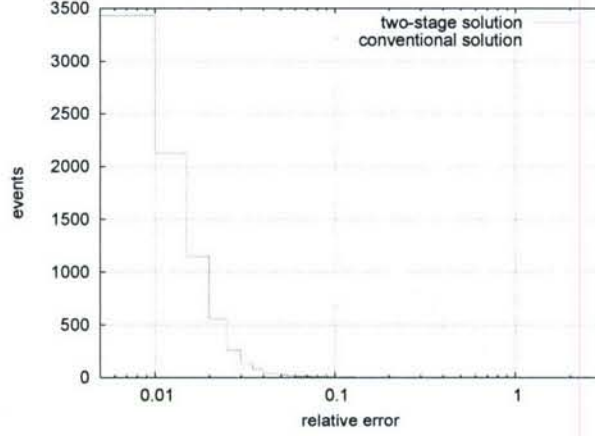
Figure 3: Distribution of the relative errors of the pressure on the section shown in Fig. 2, for the conventional and two-stage solutions.

The improved conditioning of both surface and volume problems is also indicated by the convergence histories of the iterative solutions in the conventional and two-stage approach, shown in Fig. 4. Similar examples discussed in Section 3.4 suggests that the conditioning of the matrices in the two-stage scheme is only weakly dependent on the discretization.
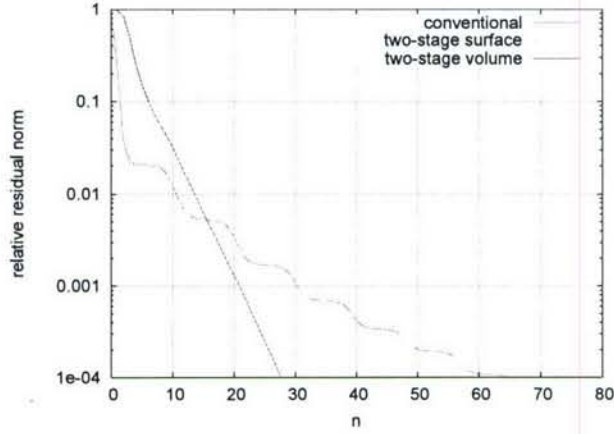
Figure 4: Convergence histories of the iterative solutions for the conventional and two-stage schemes, for the high-contrast sphere problem with $N = 200,000$.

9

3.3 Development of an FFT-based compression and fast solution methods for integral equations in acoustics

A crucial element of our approach is a fast iterative solution method utilizing a stiffness matrix compression method based on Fast Fourier Transforms (FFTs) [2]. We selected this technique rather than the Fast Multipole Method (FMM) [1], since it achieves a better performance in volumetric and low-frequency problems, i.e., in typical problems of acoustic wave propagation in biological media; it also provides a smooth and uniform transition to medium and high frequencies.

We give here a short summary of the method; the details are described in Appendix D.

The FFT-based compression method – the Adaptive Integral Method (AIM) [2] – was originally developed in the context of electromagnetics, and became one of the most widely used fast solution methods. In the present effort we modified it and applied to general (variable-density) acoustics problems.

The AIM compression relies on a decomposition of the stiffness matrix A of Eq.(3.4) into two components,

$$A = A^{\text{Near}} + A^{\text{Far}} \qquad (3.13)$$

where the "near-field" term A^{Near} describes interactions at distances of several times the spatial resolution (or average basis function support size), and "far-field" components A^{Far} is responsible for the remaining interactions. By construction, the near-field matrix A^{Near} is sparse, while the (dense) far-field matrix A^{Far} can be represented in a compressed representation, as a product of sparse matrices and a Toeplitz matrix (the latter also becomes sparse upon taking its Fourier transform, implemented as a FFT).

The compressed form of the matrix A^{Far} is obtained by representing the original basis functions (say, ϕ_α), i.e., the actual sources of the field (here, a pressure field) as "far-field-equivalent" distributions of point-like sources located on nodes of a regular Cartesian grid; the grid regularity gives rise to the Toeplitz property of the resulting far-field matrix.

More specifically, we introduce a regular Cartesian grid covering the scatterer, and characterized by some spacing h, comparable to the resolution, say a, of the problem discretization. We then approximate the original basis functions ϕ_α by sets of equivalent point sources at the nodes of an "expansion cube" C_α, defined as a set of $(M+1) \times (M+1) \times (M+1)$ grid nodes $\mathbf{u}$,

10

closest to the center of the support of the basis function,

$$\phi_\alpha(\mathbf{r}) \simeq \widehat{\phi}_\alpha(\mathbf{r}) = \sum_{\mathbf{u} \in C_\alpha} V_{\alpha\mathbf{u}} \, \delta^3(\mathbf{r} - \mathbf{u}) \, . \tag{3.14}$$

The set of the $(M+1)^3$ expansion coefficients V (strengths of the sources) is determined so that both functions, ϕ_α and $\widehat{\phi}_\alpha$, have the same **multipole moments** up to the order M. In other words, the two functions generate the same (up to the multipole order M) far fields; hence the concept of "far-field-equivalent" sources. The criterion just mentioned applies irrespectively of the relation between the discretization resolution a and the wavelength, i.e., it is valid for both high-frequency and subwavelength problems. An alternative criterion based on approximate equality of *asymptotic radiated fields* [4] may be more advantageous at higher frequencies, for which $a \gtrsim \lambda/10$.

Fig. 5 shows schematically couplings between distant and near-by tetrahedra, giving rise to matrix elements $A_{\alpha\beta}^{\text{Far}}$ and $A_{\beta\gamma}^{\text{Far}}$, as well as the expansion cubes C_α, C_β, and C_γ associated with the tetrahedra. It also indicates that the wavelength λ may be much larger than the discretization resolution.

The far-field matrix A^{Far} is then defined simply by replacing the basis functions ϕ_α in A with the basis functions $\widehat{\phi}_\alpha$. For example, if

$$A_{\alpha\beta} = \int \mathrm{d}^3 r_1 \, \mathrm{d}^3 r_2 \, \phi_\alpha(\mathbf{r}_1) \, g(\mathbf{r}_1 - \mathbf{r}_2) \, \phi_\beta(\mathbf{r}_2) \, , \tag{3.15}$$

then

$$A_{\alpha\beta}^{\text{Far}} = \int \mathrm{d}^3 r_1 \, \mathrm{d}^3 r_2 \, \widehat{\phi}_\alpha(\mathbf{r}_1) \, g(\mathbf{r}_1 - \mathbf{r}_2) \, \widehat{\phi}_\beta(\mathbf{r}_2) \equiv \sum_{\mathbf{u},\mathbf{v}} V_{\alpha\mathbf{u}} \, g(\mathbf{u} - \mathbf{v}) \, V_{\beta\mathbf{v}} \, . \tag{3.16}$$

The last expression shows that, indeed, the matrix A^{Far} is the product of two sparse matrices V and a Toeplitz matrix g. The matrix-vector multiplications $A^{\text{Near}} x$ and $A^{\text{Far}} x$ appearing in the iterative solution of the equation (3.4) can be then implemented as sequence of sparse-matrix-vector multiplications and of FFTs, with the overall storage $O(N)$ and computation cost $O(N \log N)$ (where, as before, N is the total number of unknowns).
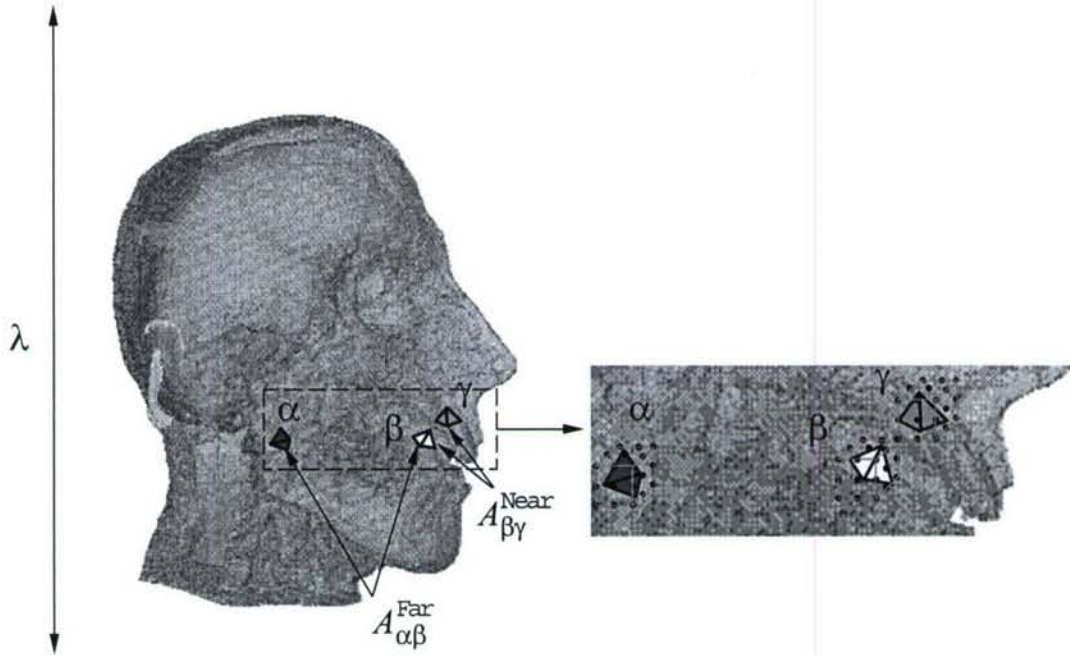
Figure 5: A schematic representation of the near- and far-field couplings
between basis functions (tetrahedra) in a model of a human head. In the
enlarged view the expansion cubes are also shown. Typical discretizations
are much finer than shown here.

In our specific problem of acoustics with variable density we use separate
expansions for the original scalar basis functions, for their gradients, and
for the gradients multiplied by material-dependent factors, as appearing in
Eqs. (3.6).

The near-field range R and the multipole expansion order M can be
adjusted (together with the grid spacing h) in order to limit the error
in the far-field to the desired level, and at the same time minimize the
computational cost and storage. In acustics problems we found that the

optimal parameters are

$$h \simeq \tfrac{1}{2}a \;, \qquad R \simeq 3\,h \;, \qquad M = 2 \;. \tag{3.17}$$

These values are, in fact, more favorable (i.e., yield lower computational costs) than in similar electromagnetic problems.

3.4 Examples and numerical results

We present below numerical results illustrating the accuracy, and the capabilities of our code. The types of problems are as follows:

- We validated the code for several problems involving homogeneous and layered spheres for the case of **constant density** (i.e., the same density of the background medium and the scatterer). We computed numerical solutions for problems from few thousand to about one million unknowns, and found that the numerical solutions approach the analytic one and remain stable with the increasing discretization density.

- We verified the accuracy and stability of our code (utilizing, in this case, the two-stage solution scheme described in Section 3.2) for a number of **large-contrast, variable-density** problems involving homogeneous and layered spheres with material properties similar to those of biological tissues.

- We performed computations for a **simple model of a human head** with the auditory channel, represented as a layered sphere with a cylindrical channel, and composed of about 800,000 tetrahedra.

- We carried out computations for a realistically shaped **model of a human head** composed of approximately 1,000,000 tetrahedra.

3.4.1 Code validation for constant-density problems

In this set of problems we considered acoustic media of the same density as the surrounding medium, i.e., $\rho(\mathbf{r}) = \rho_0$. We obtained numerical (MoM) solutions by using our fast FFT solver.

We present below results for a three-layer sphere of the outer radius of 1.0 m and the total number of unknowns of 626,561 and 376,896 corresponding to the finer and to the coarser discretizations respectively. In Table I we list the material parameters (refraction index squared, n^2) and the numbers

13

of tetrahedra in each layer. We stress that this computation was carried out only as a test of the solver, and is not mean to represent any realistic biological object in air (although it could model such an object immersed in *water*).

The tetrahedral mesh for the finer discretization is shown in Fig. 6. The sphere is excited by a plane wave of wavelength $\lambda = 2$ m.

Table 1: Parameters in the three-layer sphere problem

outer radius	n^2	N(fine)	N(coarse)
0.6 m	0.20	153,241	83,857
0.8 m	0.05	184,029	109,815
1.0 m	0.20	289,291	183,324
	total	626,561	376,896

Figure 6: One of the tetrahedral meshes (with 626,561 tetrahedra) used in the computations for the layered sphere.

In Fig. 7 we plot the far-field (scattering cross-section) obtained using the analytical solution and numerical solutions for the two discretizations given in Table 1. The curves are practically indistinguishable.

The pressure distribution inside the sphere is visualized in Fig. 8. This Figure shows an intersection of the tetrahedral mesh with a plane passing through the center of the sphere, parallel to the incident wave vector. The triangular intersections of the tetrahedra are assigned colors according to the pressure values in the tetrahedron. The maximum difference between the two numerical and the exact analytical solution is less than 3 %.

14
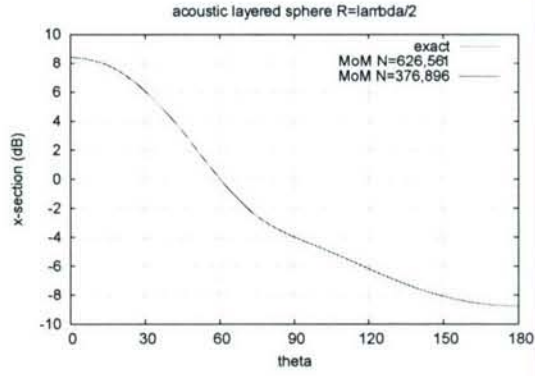
Figure 7: Comparison of the scattered field (cross-section) for the exact solution for a layered sphere and our numerical MoM solutions for $N = 626,561$ and $N = 376,896$ unknowns.
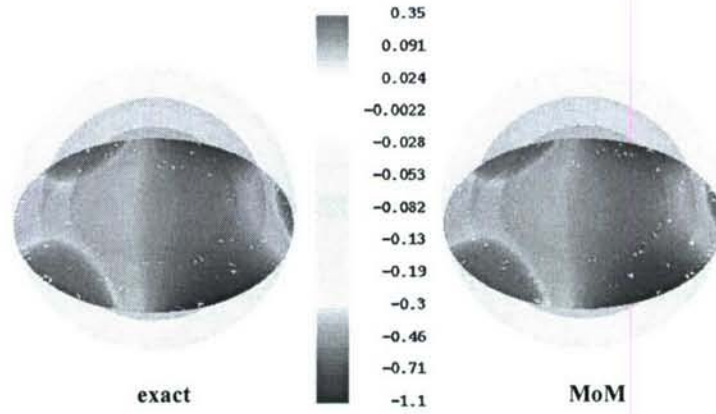
Figure 8: Comparison of pressure distributions (the imaginary part of $p(\mathbf{r})$) in a layered sphere, computed using the exact and numerical MoM solutions.

3.4.2 Code validation for variable-density, large-contrast problems

Any problem involving scattering on acoustic objects in air must necessarily involve large ratios of densities. In particular, the ratio of density of a biological tissue (or water) to that of air is above 1000. Accordingly, in our validation tests we considered such a density and the refraction index in the range $0 < n < 1$, also typical of biological media (at least for pressure waves).

Homogeneous spheres. In order to verify the accuracy of our acoustic integral-equations solver, we carried out a number of computations for either homogeneous or layered spheres, and compared the results with the exact analytical solutions, expressed as series involving Bessel functions and Legendre polynomials. The use of the developed *two-stage solution scheme* was crucial in obtaining the results, otherwise the problems would become ill-conditioned and the solutions unstable.

Figs. 9 to 10 show results for a sphere of radius $a = 10\,\text{cm}$, immersed in air, and filled with an acoustic material of the relative density $\rho/\rho_0 = 10^3$ and relative compressibility $\kappa/\kappa_0 = 10^{-4}$, corresponding to $n^2 = 0.1$ or $n \simeq 0.316$. These parameters are similar to those of bone or water (see Table 3 of Section 3.5.2). In the numerical solution we use the sphere discretization with about $N = 970,000$ tetrahedra. The sphere is excited by a plane wave of wavelength $\lambda = 60\,\text{cm}$ (i.e., of frequency $f \simeq 573\,\text{Hz}$).

The current version of the solver, partly parallelized for shared-memory (MP) platforms, was run on an SGI Origin 3900 system. The total computation time on 8 processors was about 130 minutes. The maximum required memory was about 6.4 GB.

In Fig. 9 we plot distributions of the absolute value of the pressure on a plane parallel to the incident wave vector. Fig. 10 shows the histogram of the relative error in the pressure of the numerical solution versus the analytical one. The histogram is based on 31406 events representing pressures at polygons obtained by intersecting the tetrahedral mesh with the plane of Fig. 9. It is seen that the error in the two-stage solution is of the order of 1%.

In Fig. 10 we compare the stage-1 and stage-2 convergence of the two-stage iterative solution scheme with that of the conventional scheme. The slow convergence of the conventional procedure (and the resulting large fluctuations in the pressure distributions (not shown here)) are typical symptoms of poor conditioning. These difficulties do not appear in the two-stage

16

solution approach. Incidentally, we note here that, while the convergence of conventional solution in the present problem is significanly slower than for the smaller problem with 200,000 unknowns (Fig. 4), the numbers of iterations in the two-stage scheme remain almost unchanged, which indicates that the conditioning of the surface and volume operators in Eqs. (3.8) and (3.12) is largely independent of the discretization.
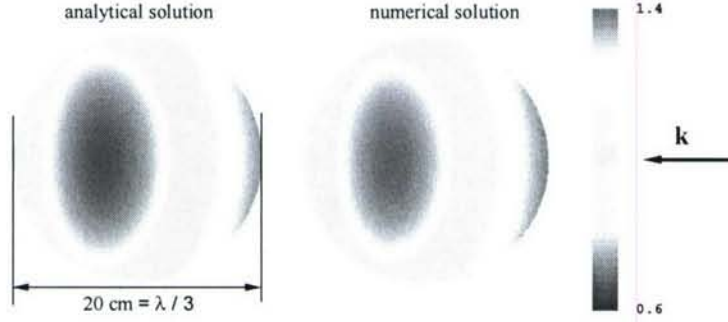
Figure 9: Distribution of the absolute value of the pressure, $|p(\mathbf{r})|$, on a plane parallel to the incident wave vector, passing through the homogeneous sphere center, computed analytically and by means of our acoustic solver, for a discretization with $N = 970,000$ tetrahedra.
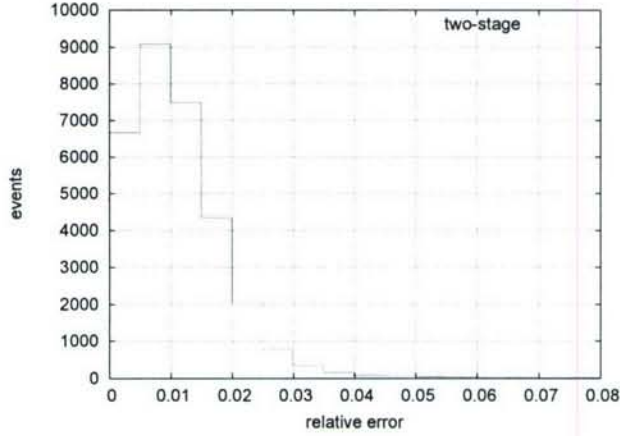
Figure 10: Histogram of the relative error in the pressure for the section shown in Fig. 9.

17
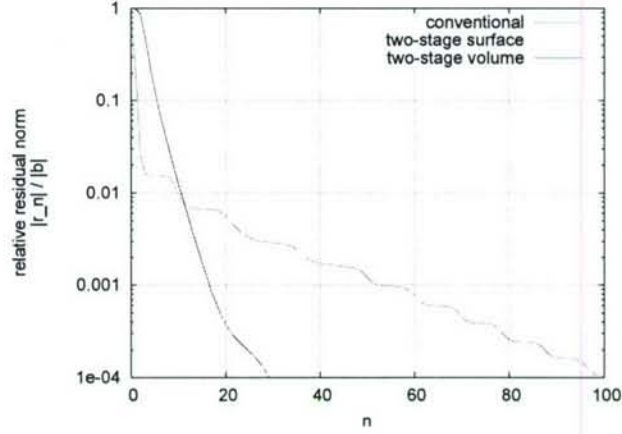
Figure 11: Convergence of the two iterative solutions in the two-stage scheme, compared to the convergence of the the conventional solution.

Multi-layered spheres. In Figs. 12 and 13 we show results for the pressure distribution in a layered sphere, with the outer shell chosen to represent the bone, and the interior of the sphere described by mechanical parameters of water (Tables 2 and 3). According to Table 3, the parameters of the inner region approximate the behavior of pressure waves in the brain tissue. As shown in Fig. 12, the outer radius of the sphere is 10 cm, and the inner radius 9 cm. We constructed a tetrahedral mesh with the tetrahedron sizes about 4 mm; hence the thickness of the shell is about three times the tetrahedron size. The total number of tetrahedra is about $N = 755,000$.
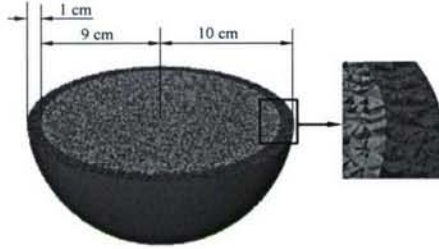
Figure 12: Discretization of the layered sphere with $N = 755,000$ tetrahedra.

Fig. 13 shows distribution of the absolute value of the pressure, $|p(\mathbf{r})|$ for the incident wave with $\lambda = 60\,\text{cm}$ (frequency $f \simeq 573\,\text{Hz}$). As in the case

18

of the homogeneous sphere, the errors in the computed pressure are of the order of 1 %.
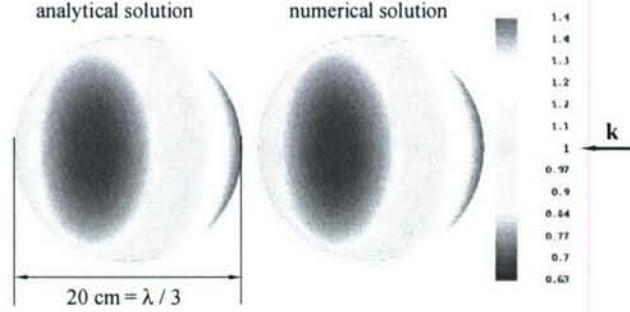
Figure 13: Distribution of the absolute value of the pressure, $|p(\mathbf{r})|$, on a plane parallel passing through the layered sphere center, computed analytically and by means of our acoustic solver, for a discretization with $N = 755,000$ tetrahedra.

3.4.3 Other variable density problems.

We present here some other representative examples illustrating capabilities of our solver in problems characterized by large density contrast.

Results for a layered sphere with a cylindrical channel. We also carried out computations for a layered sphere with a cylindrical channel – a simple model of an ear canal. The sphere size, material parameters of the layers, and the frequency are the same as in the previous example. The object is discretized with about $N = 763,000$ tetrahedra, as shown in Fig. 14. The obtained distribution of pressure is plotted in Fig. 15. The computational cost and the convergence of the solution was practically the same as in the previous examples.
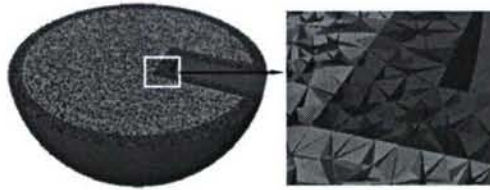
Figure 14: Discretization of the layered sphere with a channel, with $N = 763,000$ tetrahedra.

19
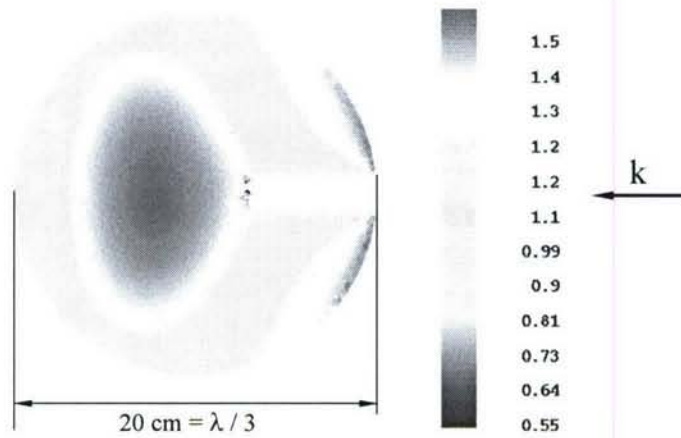
Figure 15: Distribution of the absolute value of the pressure, $|p(\mathbf{r})|$, on a plane parallel passing through the object center, computed with the discretization of Fig. 14.

Computations for a head model. As an example of a more realistic geometry, we considered a human head model, represented originally as a surface mesh with about 43,000 triangular facets (Fig. 16), and constructed a tetrahedral mesh with about $N = 1,090,000$ tetrahedra.

We took the same material parameters and the same incident wave frequency as in the previous sphere problem (i.e., $\rho/\rho_0 = 10^3$, $\kappa/\kappa_0 = 10^{-4}$, $n \simeq 0.316$, $\lambda = 60\,\mathrm{cm}$, $f \simeq 573\,\mathrm{Hz}$). At this frequency, the average edge length is about $\lambda/200$.

Fig. 17 shows the distribution of the absolute value of the pressure, $|p(\mathbf{r})|$, in the axial plane, for the indicated direction of the incident wave. As before, the solution was obtained by means of the two-stage scheme. Convergence of the solutions was similar to that in the sphere problem.

20
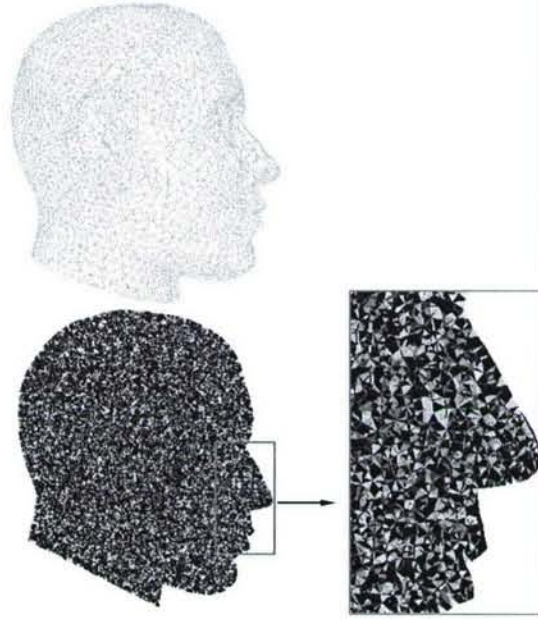
Figure 16: The surface model of the human head and its representation as a tetrahedral mesh (with $N = 1,090,000$ tetrahedra), shown in the sagittal plane cut.

20 cm = $\lambda / 3$
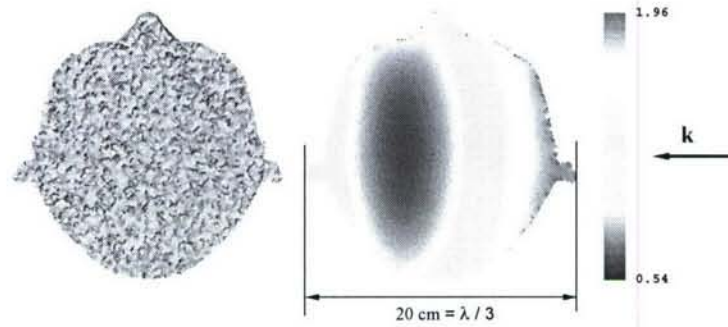
Figure 17: Distribution of the absolute value of the pressure, $|p(\mathbf{r})|$, in the axial plane, for the head model of Fig.16. The computation was done for $N = 1,090,000$ unknowns with the two-stage solution scheme. A section of the tetrahedral mesh is shown to indicate the spatial resolution.

3.5 A need for elasticity modeling

We conclude the review of our Phase I results with a discussion on the range of applicability of acoustic modeling of biological tissues, and the possible need of elastic modeling.

3.5.1 Properties of biological tissues

There exists a large body of experimental data related to biomechanics of the human head, collected in various contexts: (ultra)sound propagation, impact mechanics, neurosurgery, etc. (e.g., [5, 6]). We summarize here the most important mechanical (acoustic and elastic) properties of the relevant tissues.

Skull bones. It is generally accepted that skull bones [7] should be modeled as elastic media. It is also known that the bone properties may substantially vary between individuals, and depend on the location within the given skull. Similarly, soft tissues are usually described as elastic materials, but may be approximated as acoustic media.

Brain tissue. A mode difficult (and somewhat controversial) issue is that of the constitutive model of the brain tissues (see the review [6]). Here, within the scope of linear materials, solid or fluid, elastic, viscoelastic, or poroelastic models are being used. These models differ mainly in their long-time behavior (presence or absence of shape memory); this differences, however, are not critical in our problem, in which short-time (nearly impulsive) excitations are involved, and we do not have to describe large-time scale behavior of the system. On the other hand, correct modeling of viscous properties of the brain tissue is important in order to describe energy dissipation and thus wave attenuation in the tissue.

A related question is that of the brain tissue compressibility. Since the brain is about 83 % water by weight, it should be expected to be nearly incompressible. According to the standard set of data (Refs. [8, 9, 10, 11]), the bulk modulus of the tissue is $K \simeq 2 \cdot 10^9$ Pa, about 10^5 times larger than its shear modulus G, hence the Poisson ratio ν is very close to $\frac{1}{2}$ (see the summary of mechanical material parameters below, in Section 3.5.2).

An additional problem is a possible relevance of non-linear effects: because to the low shear wave speed in the brain tissue, material velocities may become comparable to phase (wave-front) velocity, resulting in steepening of wave-fronts, wave overturning, and similar phenomena. However,

22

while these mechanisms may be relevant in the case of large impact forces and large displacements (potentially causing head injury), they do not seem important in the context of sound conduction at amplitude levels that do not cause permanent damage to the tissues.

Sub-arachnoidal space. An important element in the human head mechanics is the sub-arachnoidal space between the skull and the brain, filled with the spongy trabeculae and cerebrospinal fluid, and cushioning the brain from shocks and vibrations. This tissue is usually modeled as a viscous solid of low shear modulus.

The properties of the tissues listed above indicate that the entire human head can be described by means of visco-elasticity equations. In the following we argue that visco-elastic modeling may be also necessary, i.e., a purely acoustic model may not reproduce important properties of the system.

3.5.2 Elastic vs. acoustic modeling of tissues

We give here a brief account of the mechanical parameters of the pertinent materials – the tissues constituting the human head. Instead of the Lamé coefficients λ_L and μ_L, we use here the bulk and shear moduli K and G,

$$K = \lambda_L + 2\mu_L = \frac{(1-\nu)E}{(1-\nu)(1-2\nu)} \; , \qquad G = \mu_L = \frac{E}{2(1+\nu)} \; , \qquad (3.18)$$

in terms of which the Young modulus and the Poisson ratio are given by

$$E = \frac{(3K-4G)G}{K-G} = \frac{(3c_P^2 - 4c_S^2)c_S^2}{c_P^2 - c_S^2} \; , \qquad (3.19a)$$

and

$$\nu = \frac{K-2G}{2(K-G)} = \frac{c_P^2 - 2c_S^2}{2(c_P^2 - c_S^2)} \; . \qquad (3.19b)$$

The corresponding speeds of sound are then

$$c_P = \sqrt{\frac{K}{\rho}} = \sqrt{\frac{(1-\nu)E}{(1+\nu)(1-2\nu)\rho}} \qquad (3.20a)$$

and

$$c_S = \sqrt{\frac{G}{\rho}} = \sqrt{\frac{E}{2(1+\nu)\rho}} \; , \qquad (3.20b)$$

23

where the subscripts P and S refer to the pressure and shear waves.

The Tables 2 and 3 below give the approximate mechanical parameters for some relevant materials. To the first approximation, soft tissues of the head (skin, muscles, etc.) have properties similar to those of water; however, properties of the brain tissue are quite different.

In the case of the brain we show both the real parts of the material parameters (in the first line), and imaginary parts (in the second line); for other tissues the imaginary parts of the parameters are much smaller. It is known that the large imaginary parts [9] are important in describing viscoelastic properties of that tissue.

In Table 3 we list indices of refraction, $n_P = c_0/c_P$ and $n_S = c_0/c_S$, relative to the environment medium (air), for which $c_0 = 344\,\text{m/s}$. The effective acoustical compressibilities κ_P and κ_S, are defined such that

$$\rho\,\kappa_P = c_P^2\,, \qquad \rho\,\kappa_S = c_S^2\,. \tag{3.21}$$

Their values, relative to the compressibility of air, as well as relative medium densities, are also listed; again, for the brain tissue, we show imaginary parts of the parameters below the real parts.[2] The parameters of Table 3 are useful in comparing elasticity problems with approximately equivalent acoustics problems.

Table 2: Mechanical properties of some materials

material	$\rho\,[\text{g/m}^3]$	$E\,[\text{Pa}]$	ν	$K\,[\text{Pa}]$	$G\,[\text{Pa}]$
air	1.2			1.42 e+05	0
water	1000		0.5	2.25 e+10	0
bone	2132.6	1.379 e+09	0.25	1.65 e+09	5.516 e+08
brain	1002.5	1.752 e+05	0.49999	2.103 e+09	5.840 e+04
Im :		−3.630 e+05	0.39 e−04	−1.613 e+05	−1.210 e+05
rubber	1100.0	8.0 e+06	0.333	1.2 e+06	3.0 e+05

---

[2]Since the brain tissue is dispersive, these quantities also depend on the frequency. The listed values correspond to 1 kHz.

Table 3: Speeds of sound, relative refraction indices, and equivalent compressibilities of some materials

material	c_P [m/s]	c_S [m/s]	n_P	n_S	ρ/ρ_0	κ_P/κ_0	κ_S/κ_0
air	344		1				
water	1500		0.22993		833.33	6.311 e−05	
bone	880.88	508.58	0.3905	0.6764	1777.2	8.5813 e−05	2.574 e−04
brain	1448.4	9.804	0.2375	25.167	835.42	6.752 e−05	0.4594
Im :	−0.0556	−6.155	9.1 e−06	15.799	835.42	5.179 e−09	0.9518
rubber	33.03	16.514	10.41	20.83	916.67	0.1183	0.4733

In addition to the material parameters of the tissues we included typical parameters of rubber, in order to contrast them with the those of the brain. Although both materials are highly elastic, the difference is that the brain tissue is nearly incompressible (hence a large bulk modulus K (Table 2), much larger than the shear modulus G), while rubber is much more compressible and its bulk modulus is only about 5 times larger than the shear modulus. As a consequence, the difference between the pressure and shear wave speeds in brain is much greater than in rubber (Table 3).

Another important aspect of the mechanical properties of the brain tissue is its viscosity, manifesting itself mostly in the large imaginary part of the shear modulus (Table 2) and, consequently, in the shear wave speed (Table 3).

3.5.3 Range of applicability of acoustic modeling of tissues

We have considered the question of what aspects of the problem of sound conduction in the human head could be described in terms of **acoustics**, without invoking elastomechanics at all. Our assessment is based on the observation that the presence of **slow shear waves** in the brain (and thus description of the brain in terms of (visco)elasticity) appears to be necessary in order to reproduce the experimentally measured resonance and antiresonance structure of the pressure distribution as a function of frequency.

One of the reasons which suggest importance of shear waves in tissues is that, if only fast pressure waves ($c_P \geq 1500\,\mathrm{m/s}$) are taken into account, the lowest resonant structure in the human skull *filled with the brain or other sort tissue* appears to arise only at about 6 kHz, while the lowest resonances

in the living skulls are observed in the vicinity of 1 kHz [12]. This fact suggests that the measured resonance structure is associated with waves of much lower speeds and thus much smaller wavelengths.

To be more precise, resonances below 1 kHz were observed also for **empty dry skulls** (or skulls artificially covered with a relatively thin layer of a damping substance [13]). However, if the shell is filled with a **low-compressibility** acoustic material (such as water), the system becomes effectively so "stiff"[3] that the lowest resonance appears only at about 7 kHz. This result suggests that, in order to generate the observed resonance structure, the material filling the shell (the skull) must support slower waves. In reality, such waves could be the **shear waves** supported by the brain tissue, of speed less than 10 m/s (Table 3).

To summarize, our assessment is that

- Purely acoustic modeling may be reasonable for (visco)elastic tissues in which the pressure wave and shear wave speeds are comparable, i.e., the the Poisson ratio ν is not too close to $\frac{1}{2}$.

- However, tissues in which the Poisson ratio is close to $\frac{1}{2}$, and in which the shear waves are much slower than the pressure waves, require full elastic modeling; it does not seem that modeling of shear waves as acoustic pressure waves can give correct results.

Consequently, we believe that the appropriate approach should be based on elasticity, or, for the brain tissues, viscoelasticity, which should include energy dissipation effects.

---

[3]i.e., the speed of sound waves becomes high.

26

Appendices

A   Integral equations in acoustics

The starting point in deriving the integral Lippmann-Schwinger equations in acoustics is the frequency-domain differential equation [3]

$$\omega^2 \kappa(\mathbf{r})\, p(\mathbf{r}) + \nabla \cdot \left(\frac{1}{\rho(\mathbf{r})}\, \nabla p(\mathbf{r}) \right) = 0 \ , \tag{A.1}$$

in which ω is the frequency, ρ the equilibrium density of the medium, and κ ist compressibility, and p the acoustic (excess) pressure.

The Lippmann-Schwinger (L-S) equation for the pressure can be obtained in the standard way from the differential equation (A.1) rewritten in the form

$$\left(k^2 + \nabla^2 \right) p - k^2 \left(1 - \frac{\kappa}{\kappa_0} \right) p - \nabla \cdot \left[\left(1 - \frac{\rho_0}{\rho} \right) \nabla p \right] = 0 \tag{A.2}$$

with

$$k = \frac{\omega}{c_0} \equiv \sqrt{\rho_0 \, \kappa_0}\, \omega \tag{A.3}$$

being the wave number of the incident wave in the background medium.

Eq.(A.2) leads [3] to the L-S equation (Eq.(3.1) in the text)

$$p^{(\text{inc})}(\mathbf{r}) = p(\mathbf{r}) + \int \mathrm{d}^3 r' \left\{ k^2\, g(\mathbf{r} - \mathbf{r}') \left(1 - \frac{\kappa(\mathbf{r}')}{\kappa_0} \right) p(\mathbf{r}') \right.$$
$$\left. - \left[\nabla_{\mathbf{r}'}\, g(\mathbf{r} - \mathbf{r}') \right] \cdot \left(1 - \frac{\rho_0}{\rho(\mathbf{r}')} \right) \nabla_{\mathbf{r}'}\, p(\mathbf{r}') \right\} \ , \tag{A.4}$$

where $p^{(\text{inc})}$ is the incident wave, satisfying the Helmholtz equation in the background medium,

$$\left(k^2 + \nabla^2 \right) p^{(\text{inc})}(\mathbf{r}) = 0 \tag{A.5}$$

and g is the corresponding Green function,

$$g(\mathbf{r}) = \frac{e^{i\,k\,|\mathbf{r}|}}{4\pi |\mathbf{r}|} \ . \tag{A.6}$$

27

Derivation of Eq.(A.4) involves the definition (A.5) of the incident wave, the standard representation theorem for the field p, and the Sommerfeld radiation condition imposed on the scattered wave $p^{(\mathrm{sc})} \equiv p - p^{(\mathrm{inc})}$.

In the main text we gave, in Eq.(3.6), two alternative expressions for the matrix elements of the stiffness matrix. The first of these was derived directly from Eq.(A.4). The second can derived by integrating by parts, or can be obtained from an alternative L-S equation

$$
p^{(\mathrm{inc})}(\mathbf{r}) = \frac{\rho_0}{\rho(\mathbf{r})}\, p(\mathbf{r}) + \int \mathrm{d}^3 r' \left\{ k^2 g(\mathbf{r} - \mathbf{r}') \left(\frac{\kappa(\mathbf{r}')}{\kappa_0} - \frac{\rho_0}{\rho(\mathbf{r}')} \right) p(\mathbf{r}') \right.
$$
$$
\left. - \left[\nabla_{\mathbf{r}'}\, g(\mathbf{r} - \mathbf{r}') \right] \cdot \left(\nabla_{\mathbf{r}'}\, \frac{\rho_0}{\rho(\mathbf{r}')} \right) p(\mathbf{r}') \right\} . \tag{A.7}
$$

which follows from the differential equation (A.2) rewritten in the form

$$
(k^2 + \nabla^2) \left(\frac{\rho_0}{\rho}\, p \right) + k^2 \left(\frac{\kappa}{\kappa_0} - \frac{\rho_0}{\rho} \right) p + \nabla \cdot \left[\left(\nabla \frac{\rho_0}{\rho} \right) p \right] = 0 . \tag{A.8}
$$

B   Discretization of integral equations in acoustics

B.1   Discretization with piecewise constant basis functions

One of the simplest choices of the basis functions in Eq.(3.3) are constant functions ϕ_α (of value, say, 1) supported on tetrahedra t_α. We also assume that the material parameters $\rho(\mathbf{r})$ and $\kappa(\mathbf{r})$ are constant within individual tetrahedra. Under these assumptions the matrix component A^{R} is diagonal, and its elements (3.6d) are proportional to the volumes of the tetrahedra. The matrix elements (3.6e) are given by integrals over tetrahedra, and the matrix elements (3.6f) are expressed as sums of integrals over faces of the tetrahedra, since gradients of the basis functions are proportional to delta-functions on the tetrahedron boundaries. Explicit expressions are

$$
A^{\mathrm{R}}_{\alpha\beta} = \delta_{\alpha\beta}\, v_\alpha\, \frac{\rho_0}{\rho_\alpha} , \tag{B.1a}
$$

$$
A^{\mathrm{M}}_{\alpha\beta} = k^2 \int\limits_{t_\alpha} \mathrm{d}^3 r_1 \int\limits_{t_\beta} \mathrm{d}^3 r_2\, g(\mathbf{r}_1 - \mathbf{r}_2) \left(\frac{\kappa_\beta}{\kappa_0} - \frac{\rho_0}{\rho_\beta} \right) , \tag{B.1b}
$$

and

28

$$A^{\mathrm{D}}_{\alpha\beta} = \int\limits_{\partial t_\alpha} \mathrm{d}^2 r_1 \int\limits_{\partial t_\beta} \mathrm{d}^2 r_2\, g(\mathbf{r}_1 - \mathbf{r}_2)\, \hat{\mathbf{n}}_\alpha(\mathbf{r}_1) \cdot \hat{\mathbf{n}}_\beta(\mathbf{r}_2)\, \Lambda(\mathbf{r}_2)$$

$$\equiv \sum_{f_\alpha \in \partial t_\alpha} \sum_{f_\beta \in \partial t_\beta} \hat{\mathbf{n}}_{f_\alpha} \cdot \hat{\mathbf{n}}_{f_\beta} \Lambda_{f_\beta} \int\limits_{f_\alpha} \mathrm{d}^2 r_1 \int\limits_{f_\beta} \mathrm{d}^2 r_2\, g(\mathbf{r}_1 - \mathbf{r}_2)\,. \qquad \text{(B.1c)}$$

In these expressions v_α is the volume of the tetrahedron t_α; ρ_α and κ_α denote values of these parameters on the tetrahedron t_α; $\hat{\mathbf{n}}_\alpha(\mathbf{r})$ is the outer unit normal to the the tetrahedron t_α; f_α is a face of the tetrahedron, and $\hat{\mathbf{n}}_{f_\alpha}$ is the outward-oriented normal to that face; finally, Λ_{f_α} is the discontinuity of the function $\rho_0/\rho(\mathbf{r})$ across the face f_α,

$$\Lambda_{f_\alpha} = \lim_{\varepsilon \to 0+} \left(\frac{\rho_0}{\rho(\mathbf{r} + \varepsilon\,\hat{\mathbf{n}}_{f_\alpha})} - \frac{\rho_0}{\rho(\mathbf{r} - \varepsilon\,\hat{\mathbf{n}}_{f_\alpha})} \right) \quad \text{for } \mathbf{r} \in f_\alpha \,. \qquad \text{(B.2)}$$

The sums over faces in Eq.(B.1c) arise because gradients of the basis functions are proportional to delta-functions on the tetrahedron boundaries. Actually, we were also able to convert volume integrals to non-singular surface integrals.

Clearly, the matrix element $A^{\mathrm{D}}_{\alpha\beta}$ is nonzero only if the tetrahedron t_β is adjacent to a surface S across which $\rho(\mathbf{r})$ is discontinuous. In particular, in the case of a single volume Ω characterized by a constant density ρ, immersed in the background medium, Eq.(B.2) yields

$$\Lambda_f = \begin{cases} 1 - \dfrac{\rho_0}{\rho} & \text{for boundary face } f \,, \\ 0 & \text{for interior face } f \,. \end{cases} \qquad \text{(B.3)}$$

We have implemented in our code discretization based on the constant basis functions described here and found that, in spite of their simplicity, accurate solutions of large problems can be obtained.

B.2 Discretization with piecewise linear basis functions.

As another choice of basis functions in acoustic L-S equations we considered scalar piecewise linear functions associated with a vertex of the tetrahedral mesh and supported on the set of tetrahedra sharing that vertex (Fig. 18). It is uniquely defined by linearity and by the requirement that $\phi_v(\mathbf{r}_v) = 1$ and $\phi_v(\mathbf{r}) = 0$ for $\mathbf{r}$ on any external face of any of the tetrahedra. It is also continuous on the region defined by $\mathcal{T}_v$.

29
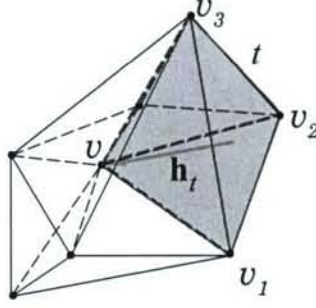
Figure 18: The set of tetrahedra supporting the basis function ϕ_v associated with the vertex v. A tetrahedron t (one of the set $\mathcal{T}_v$, consisting, in this case, of 10 tetrahedra) is shown highlighted, together with the "height vector" $\mathbf{h}_t$, normal to the face (v_1, v_2, v_3).

In the following we identify the index α in ϕ_α with the appropriate vertex number. In this formulation we also retain the previous assumption of material parameters constant on tetrahedra.

The matrix elements $A^{\mathrm{R}}_{\alpha\beta}$, $A^{\mathrm{M}}_{\alpha\beta}$, and $A^{\mathrm{D}}_{\alpha\beta}$ can be now evaluated in a similar way as for constant basis functions. One of the differences is that the material term of the matrix, A^{R}, is no longer diagonal, but remains nearly diagonal. The gradient of ϕ_α appearing in $A^{\mathrm{M}}_{\alpha\beta}$ (Eq.(3.6f)) is nonsingular, since the basis functions themselves are continuous. It can also be shown that tetrahedra adjacent to interfaces between different materials do not require any special treatment.

The advantage of the linear basis functions is that they provide a smoother solution for pressure and significantly **reduce the number of unknowns** in the problem, compared to tetrahedron-based functions. The reason is that, for typical tetrahedral meshes the number of vertices is much smaller than the number of tetrahedra, typically

$$n_v \simeq \frac{1}{5} n_t \; . \tag{B.4}$$

C A two-stage solution method

In utilizing our discretized L-S acoustics integral equations we encountered a serious difficulty associated with poor conditioning of the resulting linear system: As we discussed in Section 3.1 and in Appendix B, a peculiar feature

of the integral equation (A.7) (and thus the resulting equation involving the matrix elements (3.6)) is that, for $|\rho(\mathbf{r})/\rho_0| \gg 1$ and moderate values of the refraction index $n(\mathbf{r})$, the last (surface) term, resulting in the dipole term A^{D} in the matrix, dominates over the remaining terms. It follows that the matrix equation becomes ill-conditioned: the surface component of the solution is well defined, but the volume part of the solution (pressure in the interior of the object) is poorly determined. This is what we found numerically in applying the initial version of our solver to problems with large material density contrasts.

We were, however, able to remedy the difficulty and turn the situation to our advantage by separating the solution into its surface and volume parts, renormalizing them, and solving the problem in two stages, both without introducing any approximations (such as an expansion in ρ_0/ρ).

C.1 Reformulation of integral equations

In order to separate the surface and volume contributions to the solutions, we represent the integral equation (A.7) as

$$p^{(\mathrm{inc})} = K\,p \equiv K_{\mathrm{s}}\,p + K_{\mathrm{v}}\,p \; , \tag{C.1}$$

where the surface and volume operators are defined by

$$
\begin{aligned}
(K_{\mathrm{s}}\,p)(\mathbf{r}) &= -\int_{\partial\Omega} \mathrm{d}^2 r' \left[\hat{\mathbf{n}}(\mathbf{r}') \cdot \nabla_{\mathbf{r}'}\, g(\mathbf{r} - \mathbf{r}') \right] \Lambda(\mathbf{r}')\, p(\mathbf{r}') \\
&\equiv -\int_{\partial\Omega} \mathrm{d}^2 r' \, \frac{\partial\, g(\mathbf{r} - \mathbf{r}')}{\partial\, n(\mathbf{r}')}\, \Lambda(\mathbf{r}')\, p(\mathbf{r}')
\end{aligned} \tag{C.2a}
$$

and

$$
\begin{aligned}
(K_{\mathrm{v}}\,p)(\mathbf{r}) &= \frac{\rho_0}{\rho(\mathbf{r})}\, p(\mathbf{r}) + k^2 \int_{\overline{\Omega}} \mathrm{d}^3 r'\, g(\mathbf{r} - \mathbf{r}') \left[\frac{\kappa(\mathbf{r}')}{\kappa_0} - \frac{\rho_0}{\rho(\mathbf{r}')} \right] p(\mathbf{r}') \\
&\quad - \int_{\overline{\Omega}\backslash\partial\Omega} \mathrm{d}^3 r'\, \left[\nabla_{\mathbf{r}'}\, g(\mathbf{r} - \mathbf{r}') \right] \cdot \left(\nabla_{\mathbf{r}'}\, \frac{\rho_0}{\rho(\mathbf{r}')} \right) p(\mathbf{r}') \; .
\end{aligned} \tag{C.2b}
$$

The surface operator K_{s} of Eq.(C.2b) is defined as due to the dominant discontinuity of the density on the object boundary $\partial\Omega$; the volume operator K_{v} includes contributions due to variations of density in the interior of the object.

In the following we will obtain a set of integral equations equivalent to Eq.(C.1), but characterized by better conditioning in the limit of high object density, $\rho/\rho_0 \gg 1$. In the derivation we will utilize the standard

31

representation theorem for exterior scattering problems in acoustics,

$$p^{(\mathrm{inc})}(\mathbf{r}) + \int_{\partial\Omega} \mathrm{d}^2 r' \left[\frac{\partial g(\mathbf{r} - \mathbf{r}')}{\partial n(\mathbf{r}')} p(\mathbf{r}') - g(\mathbf{r} - \mathbf{r}') \frac{\partial p(\mathbf{r}')}{\partial n(\mathbf{r}')} \right] = \begin{cases} p(\mathbf{r}) & \text{for } \mathbf{r} \in \mathbb{R}^3 \setminus \overline{\Omega} , \\ \frac{1}{2} p(\mathbf{r}) & \text{for } \mathbf{r} \in \partial\Omega , \\ 0 & \text{for } \mathbf{r} \in \Omega . \end{cases}$$

$$(\text{C.3})$$

Eq. (C.3) is valid (under appropriate regularity conditions on the surface $\partial\Omega$, see, e.g., Ref. [14]) for any function p (here interpreted as the total pressure field) satisfying the Helmholtz equation in $\mathbb{R}^3 \setminus \overline{\Omega}$, and approaching $p^{(\mathrm{inc})}$ at infinity, in the sense that the scattered field $p^{(\mathrm{sc})} \equiv p - p^{(\mathrm{inc})}$ satisfies the Sommerfeld boundary condition,

$$\hat{\mathbf{r}} \cdot \nabla p^{(\mathrm{sc})}(\mathbf{r}) - \mathrm{i}\, k\, p^{(\mathrm{sc})}(\mathbf{r}) = o\left(|\mathbf{r}|^{-1}\right) \quad \text{for } |\mathbf{r}| \to \infty . \tag{C.4}$$

Eq.(C.3) follows, in fact, from applying the second Green identity to the functions g and $p - p^{(\mathrm{inc})}$.

Our first step in reformulating the integral equation (C.1) is to define an operator $K^{(0)}$ as the $\rho(\mathbf{r})/\rho \to \infty$ (i.e., $\Lambda(\mathbf{r}) \to 1$) limit of the surface operator K_{s},

$$\left(K^{(0)} p\right)(\mathbf{r}) = -\int_{\partial\Omega} \mathrm{d}^2 r' \frac{\partial g(\mathbf{r} - \mathbf{r}')}{\partial n(\mathbf{r}')} p(\mathbf{r}') \quad \text{for } \mathbf{r} \in \Omega ; \tag{C.5}$$

the operator $K^{(0)}$ maps functions p supported on $\partial\Omega$ onto functions defined on Ω. In terms of this operator, we then define, on the boundary $\partial\Omega$, a function $p_{\mathrm{s}}^{(0)}(\mathbf{r})$ as the solution of the surface integral equation

$$p^{(\mathrm{inc})}(\mathbf{r}) = \left(K^{(0)} p_{\mathrm{s}}^{(0)}\right)(\mathbf{r}) \quad \text{for } \mathbf{r} \in \partial\Omega_- , \tag{C.6}$$

where $\partial\Omega_- \subset \Omega$ is a surface infinitesimally close to the boundary $\partial\Omega$ and located inside the region Ω.

At the same time, if p is the solution of the exterior Neumann problem with the hard-surface boundary condition

$$\frac{\partial p^{(0)}(\mathbf{r})}{\partial n(\mathbf{r})} = 0 \quad \text{for } \mathbf{r} \in \partial\Omega , \tag{C.7}$$

and with the incident wave $p^{(\mathrm{inc})}$, the representation theorem (C.3) yields

$$p^{(\mathrm{inc})}(\mathbf{r}) + \int_{\partial\Omega} \mathrm{d}^2 r' \frac{\partial g(\mathbf{r} - \mathbf{r}')}{\partial n(\mathbf{r}')} p(\mathbf{r}') = 0 \quad \text{for } \mathbf{r} \in \Omega . \tag{C.8}$$

Eq.(C.8) is thus equivalent to Eq.(C.6), provided we identify $p_{\rm s}^{(0)}$ with p on $\partial\Omega$. It also follows that, if Eq.(C.6) holds on the surface $\partial\Omega_-$, it also holds everywhere in the region Ω, i.e., Eq.(C.6) implies

$$p^{(\rm inc)}(\mathbf{r}) = \left(K^{(0)} p_{\rm s}^{(0)}\right)(\mathbf{r}) \qquad \text{for } \mathbf{r} \in \Omega . \tag{C.9}$$

Our second step in the solution procedure is to represent the operator K as

$$K = K^{(0)} + \xi K^{(1)} \tag{C.10}$$

with

$$K^{(1)} = \xi^{-1}\left(K - K^{(0)}\right) , \tag{C.11}$$

and with the parameter ξ, depending on the function $\rho(\mathbf{r})$, chosen such that the operator $K^{(1)}$ remains finite when $|\rho(\mathbf{r})| \to \infty$. More explicitly

$$
\begin{aligned}
(K^{(1)} p)(\mathbf{r}) = &\int_{\partial\Omega} \mathrm{d}^2 r' \, \frac{\partial \, g(\mathbf{r} - \mathbf{r}')}{\partial \, n(\mathbf{r}')} \frac{\rho_0}{\xi \, \rho(\mathbf{r}')} p(\mathbf{r}') \\
&+ \frac{\rho_0}{\xi \, \rho(\mathbf{r})} p(\mathbf{r}) + k^2 \int_{\overline{\Omega}} \mathrm{d}^3 r' \, g(\mathbf{r} - \mathbf{r}') \frac{1}{\xi}\left[\frac{\kappa(\mathbf{r}')}{\kappa_0} - \frac{\rho_0}{\rho(\mathbf{r}')}\right] p(\mathbf{r}') \\
&- \int_{\overline{\Omega}\backslash\partial\Omega} \mathrm{d}^3 r' \, \left[\nabla_{\mathbf{r}'} \, g(\mathbf{r} - \mathbf{r}')\right] \cdot \left(\nabla_{\mathbf{r}'} \frac{\rho_0}{\xi \, \rho(\mathbf{r}')}\right) p(\mathbf{r}') ,
\end{aligned}
$$

and we can choose ξ, e.g., as the average value of $\rho_0/\rho(\mathbf{r})$ over the region Ω,

$$\xi \sim \left\langle \frac{\rho_0}{\rho} \right\rangle_\Omega . \tag{C.12}$$

Having specified the operators $K^{(0)}$ and $K^{(1)}$, and the solution $p_{\rm s}^{(0)}$, we represent the full solution as

$$p = p_{\rm s}^{(0)} + \xi p_{\rm s}^{(1)} + p_{\rm v} , \tag{C.13}$$

where $p_{\rm s}^{(1)}$ is the correction to the surface solution $p_{\rm s}^{(0)}$ and $p_{\rm v}$ is the volume part of the solution, defined such that

$$K^{(0)} p_{\rm v} = K_{\rm s} p_{\rm v} = 0 . \tag{C.14}$$

By substituting Eqs. (C.10) and (C.13) into Eq.(C.1) and making use of Eqs. (C.6), (C.9), and (C.14), we find the **volumetric equation**

$$\left(\left[K^{(0)} + \xi K^{(1)}\right] p_{\rm s}^{(1)}\right)(\mathbf{r}) + \left(K^{(1)} p_{\rm v}\right)(\mathbf{r}) = -\left(K^{(1)} p_{\rm s}^{(0)}\right)(\mathbf{r}) \quad \text{for } \mathbf{r} \in \overline{\Omega} \tag{C.15}$$

33

for the unknown fields $p_{\mathrm{s}}^{(1)}$ and p_{v}, with the r.h.s. expressed in terms of the previously determined surface problem solution $p_{\mathrm{s}}^{(0)}$.

The solution procedure amounts then to solving the surface equation (C.6), the volumetric equation (C.15), and forming the final solution according to Eq.(C.13), as described in Section 3.2.

We stress the importance of Eq.(C.9) (i.e., extension of Eq.(C.6) to the interior of the region Ω) in the derivation of Eq.(C.15). Eq.(C.9) is necessary for cancellation of large terms $\sim \xi^{-1}$, which would be otherwise present in Eq.(C.15).

C.2 Solution of the discretized problem

In the discretized problem, the counterpart of the solution procedure described above is as follows:

In analogy to the integral operator decomposition (C.10), we represent the stiffness matrix of Eq. (3.6) as

$$A \equiv A^{\mathrm{R}} + A^{\mathrm{M}} + A^{\mathrm{D}} = A^{(0)} + \xi\, A^{(1)}\ , \qquad (\mathrm{C}.16)$$

where the elements of the matrices $A^{(0)}$ and $A^{(1)}$ are given, explicitly, by

$$A_{\alpha\beta}^{(0)} = -\int_{\overline{\Omega}} \mathrm{d}^3 r_1 \int_{\partial\Omega} \mathrm{d}^2 r_2 \left[\nabla_{\mathbf{r}_1}\phi_\alpha(\mathbf{r}_1)\right] g(\mathbf{r}_1 - \mathbf{r}_2) \cdot \hat{\mathbf{n}}(\mathbf{r}_2)\,\phi_\beta(\mathbf{r}_2)\ , \qquad (\mathrm{C}.17\mathrm{a})$$

and

$$
\begin{aligned}
A_{\alpha\beta}^{(1)} ={}& \int_{\overline{\Omega}} \mathrm{d}^3 r_1 \int_{\partial\Omega} \mathrm{d}^2 r_2 \left[\nabla_{\mathbf{r}_1}\phi_\alpha(\mathbf{r}_1)\right] g(\mathbf{r}_1 - \mathbf{r}_2) \cdot \hat{\mathbf{n}}(\mathbf{r}_2)\,\frac{\rho_0}{\xi\,\rho(\mathbf{r}_2)}\,\phi_\beta(\mathbf{r}_2) \\
&+ \int \mathrm{d}^3 r\, \phi_\alpha(\mathbf{r})\,\frac{\rho_0}{\xi\,\rho(\mathbf{r})}\,\phi_\beta(\mathbf{r}) \\
&+ k^2 \int \mathrm{d}^3 r_1\, \mathrm{d}^3 r_2\, \phi_\alpha(\mathbf{r}_1)\, g(\mathbf{r}_1 - \mathbf{r}_2)\,\frac{1}{\xi}\left[\frac{\kappa(\mathbf{r}_2)}{\kappa_0} - \frac{\rho_0}{\rho(\mathbf{r}_2)}\right]\phi_\beta(\mathbf{r}_2) \\
&- \int_{\overline{\Omega}} \mathrm{d}^3 r_1 \int_{\overline{\Omega}\backslash\partial\Omega} \mathrm{d}^3 r_2 \left[\nabla_{\mathbf{r}_1}\phi_\alpha(\mathbf{r}_1)\right] g(\mathbf{r}_1 - \mathbf{r}_2) \cdot \left(\nabla_{\mathbf{r}_2}\frac{\rho_0}{\xi\,\rho(\mathbf{r}_2)}\right)\phi_\beta(\mathbf{r}_2)\ .
\end{aligned}
$$

$$(\mathrm{C}.17\mathrm{b})$$

We note that, when $\rho(\mathbf{r})/\rho_0 \to \infty$ uniformly in the volume Ω and ξ is defined by Eq.(C.12), the matrices $A^{(0)}$ and $A^{(1)}$ remain finite.

It is clear from Eq.(C.17b) that the matrix elements $A_{\alpha\beta}^{(0)}$ may be nonzero only for basis functions ϕ_β overlapping the boundary $\partial\Omega$ of the object. We

call these basis functions **"surface"** basis functions, and the remaining ones **"volume"** basis functions, and, accordingly, decompose the matrix (C.16) into blocks as

$$A = A^{(0)} + \xi A^{(1)} = \begin{bmatrix} A_{ss}^{(0)} + \xi A_{ss}^{(1)} & \xi A_{sv}^{(1)} \\ A_{vs}^{(0)} + \xi A_{vs}^{(1)} & \xi A_{vv}^{(1)} \end{bmatrix} , \tag{C.18}$$

where we used the fact that, by construction, the elements $A_{\alpha\beta}^{(0)}$ are nonzero only for "surface" column indices β (cf. Eq.(C.14)).

Similarly, we decompose the solution vector x (Eq.(3.3)) into "surface" and "volume" blocks as

$$x = \begin{bmatrix} x_s \\ x_v \end{bmatrix} = \begin{bmatrix} x_s^{(0)} + \xi x_s^{(1)} \\ x_v \end{bmatrix} , \tag{C.19}$$

where we **define** $x_s^{(0)}$ as the solution of the equation

$$A_{ss}^{(s)} x_s^{(0)} = b_s ; \tag{C.20}$$

here b_s is the surface block of the r.h.s. vector b

$$b = \begin{bmatrix} b_s \\ b_v \end{bmatrix} . \tag{C.21}$$

If we now substitute Eqs. (C.18), (C.19), and (C.21) into the original equation

$$A x = b , \tag{C.22}$$

and use Eq.(C.20), we obtain the system of equations

$$\left(A_{ss}^{(0)} + \xi A_{ss}^{(1)} \right) x_s^{(1)} + A_{sv}^{(1)} x_v = -A_{ss}^{(1)} x_s^{(0)} , \tag{C.23a}$$

$$\left(A_{vs}^{(0)} + \xi A_{vs}^{(1)} \right) x_s^{(1)} + A_{vv}^{(1)} x_v = -A_{vs}^{(1)} x_s^{(0)} + \xi^{-1} \left(b_v - A_{vs}^{(0)} x_s^{(0)} \right) , \tag{C.23b}$$

where the r.h.s.s are expressed in terms of the solution of Eq.(C.20).

As in the derivation of Eq.(C.15) in the previous Section, we now have to show that Eq.(C.20) implies

$$A_{vs}^{(0)} x_s^{(0)} = b_v ; \tag{C.24}$$

and both these equations are just the discrete counterparts of Eqs. (C.6) and (C.9), obtained by expanding the field $p^{(0)}$ into the basis functions ϕ_α (Eq.(3.3)) and projecting on the same set of basis functions.

It follows then from Eq.(C.24) that Eqs. (C.23) reduce to

$$
\begin{bmatrix} A_{ss} & A_{sv}^{(1)} \\ A_{vs} & A_{vv}^{(1)} \end{bmatrix} \begin{bmatrix} x_s^{(1)} \\ x_v \end{bmatrix} = - \begin{bmatrix} A_{ss}^{(1)} x_s^{(0)} \\ A_{vs}^{(1)} x_s^{(0)} \end{bmatrix} \equiv \widehat{b} .
\tag{C.25}
$$

We note that the solution depends on the original r.h.s. b only through its surface block b_s appearing in Eq.(C.20).

Thus, finally, the solution procedure for the discretized equations is the exact counterpart of the procedure described in Section C.1 following Eq.(C.15):

1. solve the **surface** problem (C.20);

2. by using the solution $x_s^{(0)}$, compute the r.h.s. of Eq.(C.25),

3. solve the **volumetric** problem (C.25) for $x_s^{(1)}$ and x_v; and

4. construct the full solution according to Eq.(C.19).

C.3   Implementation in the code

We have implemented the above two-stage (surface + volume) solution procedure in our code; some representative results were described in Section 3.4. This approach enabled us to obtain accurate solutions for practical problems with large ρ/ρ_0; when using the original formulation, we were not able to generate a meaningful solution due to instabilities caused by ill-conditioning.

In the present implementation of the algorithm we construct the matrices $A^{(0)}$ and $A^{(1)}$ just by modifying the input to the construction of the full matrix A. Further, instead of solving Eq.(C.25), we solve an equivalent equation involving the original matrix A and a "right preconditioner" – an additional diagonal matrix (denoted Q) which effectively rescales the columns of the matrix A. We describe these element of the implementation below:

Construction of the matrices $A^{(0)}$ and $A^{(1)}$. The code uses as input two quantities characterizing material properties of the object:

$$
\gamma_\kappa(\mathbf{r}) = \frac{\kappa(\mathbf{r})}{\kappa_0} - 1 , \qquad \gamma_\rho(\mathbf{r}) = 1 - \frac{\rho_0}{\rho(\mathbf{r})} .
\tag{C.26}
$$

36

In terms of these functions, the matrix elements of Eqs. (3.6d) – (3.6f) can be written as

$$
\begin{aligned}
A_{\alpha\beta} = & \int d^3r\, \phi_\alpha(\mathbf{r}) \left[1 - \gamma_\rho(\mathbf{r})\right] \phi_\beta(\mathbf{r}) \\
& + k^2 \int d^3r_1\, d^3r_2\, \phi_\alpha(\mathbf{r}_1)\, g(\mathbf{r}_1 - \mathbf{r}_2) \left[\gamma_\kappa(\mathbf{r}_2) + \gamma_\rho(\mathbf{r}_2)\right] \phi_\beta(\mathbf{r}_2) \quad \text{(C.27)} \\
& + \int d^3r_1\, d^3r_2\, \left[\nabla_{\mathbf{r}_1} \phi_\alpha(\mathbf{r}_1)\right] g(\mathbf{r}_1 - \mathbf{r}_2) \cdot \left[\nabla_{\mathbf{r}_2} \gamma_\rho(\mathbf{r}_2)\right] \phi_\beta(\mathbf{r}_2) \,.
\end{aligned}
$$

It can be now easily checked that the matrices $A^{(0)}$ and $A^{(1)}$ of Eqs. (C.17) are obtained from the general equation (C.27) with the functions γ_κ and γ_ρ replaced, respectively, by

$$
\gamma_\kappa^{(0)}(\mathbf{r}) = -1\,, \qquad \gamma_\rho^{(0)}(\mathbf{r}) = 1 \tag{C.28}
$$

(corresponding to $\kappa(\mathbf{r}) = 0$ and $\rho(\mathbf{r}) = \infty$) and by

$$
\gamma_\kappa^{(1)}(\mathbf{r}) = \frac{1}{\xi}\left[1 + \gamma_\kappa(\mathbf{r})\right] - 1 \equiv \frac{\kappa(\mathbf{r})}{\xi\,\kappa_0} - 1\,, \tag{C.29a}
$$

$$
\gamma_\rho^{(1)}(\mathbf{r}) = 1 - \frac{1}{\xi}\left[1 - \gamma_\rho(\mathbf{r})\right] \equiv 1 - \frac{\rho_0}{\xi\,\rho(\mathbf{r})}\,. \tag{C.29b}
$$

Construction of the rescaled volumetric equation.   We note that the matrix appearing in Eq.(C.25) can be represented as

$$
\begin{bmatrix} A_{ss} & A_{sv}^{(1)} \\ A_{vs} & A_{vv}^{(1)} \end{bmatrix} = \begin{bmatrix} A_{ss} & \xi A_{sv}^{(1)} \\ A_{vs} & \xi A_{vv}^{(1)} \end{bmatrix} \begin{bmatrix} I & 0 \\ 0 & \xi^{-1} I \end{bmatrix} \equiv AQ\,. \tag{C.30}
$$

(cf. Eq.(C.18)). Therefore, instead of solving Eq.(C.25) we solve the equation

$$
AQ \begin{bmatrix} x_s^{(1)} \\ x_v \end{bmatrix} = \widehat{b} \tag{C.31}
$$

involving the original matrix A and the diagonal matrix Q playing the role of a "right preconditioner".

D   A fast solution method for integral equations in acoustics

In view of the complexity of the anatomical models of the human head and the resulting problem sizes (up to millions of unknowns), compression of the

37

stiffness matrix and a fast solution method are necessities. In Phase I we implemented an extension of the FFT-based (AIM) matrix compression [2] to acoustics.

We first present the formulation of the method in its application to acoustics, and then describe its implementation in our code.

D.1   General formulation

The AIM approach simply amounts to replacing, in computation of elements of the stiffness matrix,[4] the MoM basis functions (such as the functions ϕ_α in Eqs. (3.3) and (3.6)) by sets of "approximately equivalent" auxiliary point sources located at nodes of a regular Cartesian grid. The "equivalence" is understood in the sense that the two source representations generate the same (to the desired tolerance) far field. Depending on the equation type, we apply the equivalent source expansion to the scalar basis functions and their gradients (Eq.(3.6)), to individual components the vector basis functions, say ψ_α, to their divergences, derivatives in the tensors, etc.

To simplify the notation, we denote in the following by φ any of those basis functions or their components,

$$\varphi_\alpha(\mathbf{r}) = \begin{cases} \phi_\alpha(\mathbf{r})\,, \\ \nabla \phi_\alpha(\mathbf{r})\,, \\ \psi_\alpha^i\,, \\ \nabla \cdot \psi_\alpha(\mathbf{r})\,, \\ \frac{1}{2}\left[\partial_i\, \psi_\alpha^j(\mathbf{r}) + \partial_j\, \psi_\alpha^i(\mathbf{r})\right]\,, \\ \cdots\,. \end{cases} \tag{D.1}$$

In the case of the scalar basis functions the index α refers to tetrahedra (for constant basis functions) or vertices (for linear basis functions), etc.

The compression procedure is as follows:

1. We construct a regular Cartesian grid $\mathcal{G}$ of node spacing h, covering the scatterer, and select a multipole expansion order $M = 0, 1, 2, \ldots$.

2. Then, for each basis function φ_α define a cube-shaped set C_α (which we call the "expansion cube") consisting of $(M + 1)^3$ Cartesian grid nodes $\mathbf{u} \in \mathcal{G}$, and covering[5] in the optimal way (according to predefined

---

[4]More precisely, the replacement is done in the terms involving the Green function.
[5]We have to require here that Mh is larger than than the diameter of the basis function support.

geometrical criteria) the basis function support. For example, we may require that the center $\mathbf{c}_\alpha$ of the cube C_α is located closest to the centroid of the basis function support (the center $\mathbf{c}_\alpha$ would coincide with one of grid nodes for M even, and with a grid cell center for M odd).

3. We approximate the original basis function φ_α by a set of equivalent point sources at the nodes of the expansion cube C_α,

$$\varphi_\alpha(\mathbf{r}) \simeq \widehat{\varphi}_\alpha(\mathbf{r}) = \sum_{\mathbf{u} \in C_\alpha} V_{\alpha\mathbf{u}} \, \delta^3(\mathbf{r} - \mathbf{u}) \,, \tag{D.2}$$

where the set of $(M+1)^3$ coefficients V (strengths of the sources) is determined so that both functions have the same the multipole moments up to the order M, i.e.,

$$\int d^3\rho \, \rho^{\mathbf{m}} \left[\varphi_\alpha(\mathbf{c}_\alpha + \rho) - \widehat{\varphi}_\alpha(\mathbf{c}_\alpha + \rho) \right]$$
$$\equiv \int d^3\rho \, \rho_x^{m_x} \rho_y^{m_y} \rho_z^{m_z} \left[\varphi_\alpha(\mathbf{c}_\alpha + \rho) - \widehat{\varphi}_\alpha(\mathbf{c}_\alpha + \rho) \right] \tag{D.3}$$
$$= 0 \qquad \text{for } 0 \le m_x, m_y, m_z \le M \,.$$

Here and below we use the multi-index notation with $\mathbf{m} = (m_x \, m_y \, m_z)$, and the multipole moments are evaluated relative to the center $\mathbf{c}_\alpha$ of the expansion cube.

In order to find the set of $(M + 1)^3$ coefficients V

(a) We evaluate the set of $(M + 1)^3$ multipole moments up to the order M,

$$\langle \varphi_\alpha \rangle_{\mathbf{m}}(\mathbf{c}_\alpha) = \int d^3\rho \, \rho^{\mathbf{m}} \, \varphi_\alpha(\mathbf{c}_\alpha + \rho) \qquad \text{for } 0 \le m_x, m_y, m_z \le M \tag{D.4}$$

of the basis functions with respect to the expansion cube center $\mathbf{c}_\alpha$.

(b) We solve the set of $(M + 1)^3$ equations

$$\sum_{\mathbf{u} \in C_\alpha} (\mathbf{u} - \mathbf{c}_\alpha)^{\mathbf{m}} V_{\alpha\mathbf{u}} = \langle \varphi_\alpha \rangle_{\mathbf{m}}(\mathbf{c}_\alpha) \qquad \text{for } 0 \le m_x, m_y, m_z \le M \,. \tag{D.5}$$

39

Eq.(D.5) is the Vandermonde system, and its well-known closed-form solution is given, e.g., in Ref.[2] and in Appendix B.2 of our Status Report 2.

4. In the near-field range we compute the matrix elements according to the original MoM expression (such as (3.6)), while in the far-field range we utilize the expansion (D.2) for the basis functions. This yields the representation of the matrix elements

$$a_{\alpha\beta} \simeq a_{\alpha\beta}^{\mathrm{Near}} + a_{\alpha\beta}^{\mathrm{Far}} \tag{D.6}$$

where

$$a_{\alpha\beta}^{\mathrm{Near}} = \begin{cases} a_{\alpha\beta} - a_{\alpha\beta}^{\mathrm{Far}} & \text{for } \mathrm{dist}(C_\alpha - C_\beta) \leq dh \text{ and } \dfrac{|a_{\alpha\beta} - a_{\alpha\beta}^{\mathrm{Far}}|}{|a_{\alpha\beta}|} \geq \epsilon, \\ 0 & \text{otherwise} \end{cases}$$

$$\tag{D.7}$$

and

$$a_{\alpha\beta}^{\mathrm{Far}} = \sum_{\substack{\mathbf{u} \in C_\alpha, \mathbf{v} \in C_\beta \\ \mathbf{u} \neq \mathbf{v}}} V_{\alpha\mathbf{u}}\, g(\mathbf{u} - \mathbf{v})\, V_{\beta\mathbf{v}} . \tag{D.8}$$

In Eq.(D.7) $\mathrm{dist}(\cdots)$ denotes the distance between the expansion cubes,

$$\mathrm{dist}(C_\alpha - C_\beta) = \min_{\mathbf{u} \in C_\alpha, \mathbf{v} \in C_\beta} \|\mathbf{u} - \mathbf{v}\| \tag{D.9}$$

and the distance $\| \cdot \|$ (in fact, the $\| \cdot \|_\infty$ norm) is defined by

$$\|\mathbf{u}\| = \max\{|u_x|, |u_y|, |u_z|\} . \tag{D.10}$$

The integer parameter d in Eq.(D.7) is the **near-field range**, and the parameter $\epsilon > 0$ is the **near-field tolerance**. Eq.(D.7) states that in the near-field range the matrix element $a_{\alpha\beta}$ is replaced by the difference of its exact value and the far-field approximation $a_{\alpha\beta}^{\mathrm{Far}}$, unless the approximation is accurate to the tolerance ϵ. The subtraction of the far-field term is necessary, since, for arbitrary locations of the basis function supports, there is no translationally invariant way of expressing the geometrical near-field condition in Eq.(D.7) [6] – and the factorized, translationally invariant form of Eq.(D.8) is the crucial

---

[6]We note that, on the other hand, the restriction $\mathbf{u} \neq \mathbf{v}$ in Eq.(D.8) is equivalent to the translationally invariant condition $g(\mathbf{0}) = 0$.

element of the representation. In fact, the far-field part (D.8) of the matrix is a product of the Toeplitz matrix G of elements $g(\mathbf{u} - \mathbf{v})$, and the sparse matrix V and its transpose; clearly, the Toeplitz property allows computation of the matrix-vector product by means of Fast Fourier Transform (FFT). Since, by construction, the near-field part (D.7) of the matrix is sparse, Eq.(D.6) provides a compressed representation of the original matrix.

For the given geometry and its MoM discretization, the error due to the matrix compression (Section D.4) and the computational cost (Section D.6) are controlled by the parameters h, d, and M, i.e., the Cartesian grid spacing, the near-field range, and the multipole expansion order. We discuss later on the optimal choice of these parameters, ensuring the desired accuracy and minimizing the computational cost.

D.2   Application to specific integral operators in acoustics

We present here applications of the AIM compression to some specific integral operators and their discretized representations.

Constant basis functions.   In this case we apply AIM compression to the monopole and dipole matrices of Eqs. (B.1). In the first of these we use the expansion

$$\phi_\alpha(\mathbf{r}) \simeq \widehat{\phi}_\alpha(\mathbf{r}) = \sum_{\mathbf{u} \in C_\alpha} V^{\mathrm{M}}_{\alpha\mathbf{u}} \delta^3(\mathbf{r} - \mathbf{u}) \tag{D.11}$$

for the basis functions constant on tetrahedra α, where the expansion coefficients V^{M} are evaluated as described in Appendices B.1 (evaluation of the multipole moments) and B.2 (solution of the Vandermonde system (D.5)) of our Status Report 2.
We obtain in this way the far-field approximation

$$A^{\mathrm{M}}_{\alpha\beta} \simeq k^2 \sum_{\mathbf{u},\mathbf{v}} V^{\mathrm{M}}_{\alpha\mathbf{u}} \, g(\mathbf{u} - \mathbf{v}) \, V^{\mathrm{M}}_{\beta\mathbf{v}} \left(\frac{\kappa_\beta}{\kappa_0} - \frac{\rho_0}{\rho_\beta} \right) . \tag{D.12}$$

Similarly, in the dipole term we approximate the gradient of the basis function and its product with the material-dependent function Λ

$$\nabla\phi_\alpha(\mathbf{r}) \simeq \sum_{\mathbf{u} \in C_\alpha} \mathbf{V}^{\mathrm{D}}_{\alpha\mathbf{u}} \delta^3(\mathbf{r} - \mathbf{u}) \tag{D.13a}$$

and

41

$$\nabla \phi_\alpha(\mathbf{r}) \, \Lambda(\mathbf{r}) \simeq \sum_{\mathbf{u} \in C_\alpha} \mathbf{V}_{\alpha\mathbf{u}}^{D\Lambda} \, \delta^3(\mathbf{r} - \mathbf{u}) \quad . \tag{D.13b}$$

We find in this way

$$A_{\alpha\beta}^D \simeq \sum_{\mathbf{u},\mathbf{v}} \mathbf{V}_{\alpha\mathbf{u}}^D \, g(\mathbf{u} - \mathbf{v}) \cdot \mathbf{V}_{\beta\mathbf{v}}^{D\Lambda} \quad , \tag{D.14}$$

where the vector-valued expansion coefficients $\mathbf{V}^D$ and $\mathbf{V}^{D\Lambda}$ are given by

$$\mathbf{V}_{\alpha\mathbf{u}}^D = \sum_{f_\alpha \in \partial t_\alpha} \hat{\mathbf{n}}_{f_\alpha} \, V_{f_\alpha \mathbf{u}} \tag{D.15a}$$

and

$$\mathbf{V}_{\alpha\mathbf{u}}^{D\Lambda} = \sum_{f_\alpha \in \partial t_\alpha} \hat{\mathbf{n}}_{f_\alpha} \, \Lambda_{f_\alpha} \, V_{f_\alpha \mathbf{u}} \quad ; \tag{D.15b}$$

here $V_{f\mathbf{u}}$ are expansion coefficients for a constant basis function supported on the triangular face f, the sums are taken over all faces of the considered tetrahedra. We note that the expansion coefficients $\mathbf{V}^{D\Lambda}$ depend on the discontinuities Λ of the material parameter ρ_0/ρ on the individual faces. In this way, Eqs. (D.12) and (D.14) provide a compressed matrix representation on terms of scalar expansion coefficients V^M and two sets of vector expansion coefficients, $\mathbf{V}^D$ and $\mathbf{V}^{D\Lambda}$ (hence, the total of 7 components). Explicit expressions for the vectorial expansion coefficients can be obtained by computing the multipole moments of gradients of the basis functions and solving the resulting Vandermonde system. Such results are given in Ref. [2]; we also provided specific expression for the acoustics problems in our Status Report 2.

We also note that the expansion coefficients $\mathbf{V}_{\alpha\mathbf{u}}^D$ of Eq.(D.15) represent the *gradient* $\nabla\phi_\alpha$ of the basis function ϕ_α. Therefore, the zero-th order (monopole) of the far-field-equivalent basis function (D.13a) must vanish exactly; this requires a high numerical precision in evaluating the coefficients $\mathbf{V}^D$ and the pertinent far-field expansions. A possible alternative way of parameterizing the FFT-compressed matrix could be to use *dipole* rather than monopole point sources, which would then automatically guarantee vanishing of the monopole component of the far-field. On the other hand, the expansion (D.13b) will, generally, yield a nonvanishing monopole moment, and will be easier to handle numerically.

Linear basis functions. The structure of the basis function and matrix element expansions is here the same as in Eqs. (D.11) to (D.15b). Explicit

expressions for the expansion coefficients can be obtained by computing the multipole moments of gradients of the basis functions as described in Appendix B.1.3 of our Status Report 2.

D.3 Geometry and discretization

Since we are concerned with acoustic wave propagation in biological media, we concentrate on volumetric problems, assuming an approximately uniform distribution of the material in the considered volume. For the purpose of algorithm complexity estimates, we introduce the following quantities and notation:

1. We consider an object (e.g., a cube) of linear sizes $L \times L \times L$ uniformly discretized with the **spatial resolution** a. The number of MoM unknowns is then

$$N \simeq c_V \left(\frac{L}{a}\right)^3 \qquad (D.16)$$

with a coefficient c_V dependent on the discretization. E.g., for the case of partition into regular cubes, with each of them partitioned into a minimum number of tetrahedra, we have $c_V = 5$. We stress that, in this context, the parameter a controls merely the **number of unknowns** per unit volume of the scatterer. We only assume that the sizes of basis function supports are not larger than a.

2. We introduce a regular Cartesian grid $\mathcal{G}$ of $K \times K \times K$ nodes with the cell size, or **grid spacing** h, hence $K = L/h$. Therefore, the number of grid nodes is

$$N_{\mathcal{G}} = K^3 = \left(\frac{L}{h}\right)^3 . \qquad (D.17)$$

We allow the grid spacing h to be large relative to the geometry spatial resolution b; however, we will find that the optimal grid spacing is comparable to a.

3. With the partition specified above, the number of unknowns n_C per grid cell is then, on the average,

$$n_C = \frac{N}{N_{\mathcal{G}}} \simeq c_V \left(\frac{h}{a}\right)^3 . \qquad (D.18)$$

43

D.4 Error estimates

Since we are mostly concerned here with subwavelength problems, we can determine approximate error bounds by neglecting the oscillatory behavior of the Green function (3.2) altogether, i.e., considering the Laplace equation Green function

$$g_0(\mathbf{r}) = \frac{1}{4\pi |\mathbf{r}|} \, . \tag{D.19}$$

The estimates we obtain remain valid as long as the basis function supports and the Cartesian grid spacing h are small compared to the wavelength. We use the assumptions about the geometry and its discretization as specified in Section D.3.

The error in the matrix elements due to the approximation (D.2) is controlled by the (integer) near-field range d and the multipole expansion order M. According to the definition of the range d in Eqs. (D.7) and (D.9), the minimum far-field distance between the centers of the expansion cubes is

$$R_{\min}^{\mathrm{AIM}}(d, M) = (d + M)\, h \tag{D.20}$$

(we recall that the cube size is $M\, h$). A qualitative estimate of the error in the matrix elements due to the multipole approximation (D.2) is

$$e_{\mathrm{AIM}}(d, M) \sim \left(\frac{1}{d + M}\right)^{M+1} . \tag{D.21}$$

However, since the coefficient in this estimate is not easy to determine analytically, we use numerical data.

In Fig. 19 we show the computed relative errors in matrix elements for **scalar** piecewise constant functions ϕ_α (Appendix B.1), computed for expansion orders $M = 2, 3, 4$, and for grid spacing h equal to the basis function support size a. The errors are plotted as functions of the distance R between the expansion cubes (measured in the grid spacing units h), and the expansion order M, for typical values of the grid spacing relative to the basis function support sizes. The plot is based on a statistical sample of matrix elements for various distances and orientations of the basis functions' supports. The errors depend somewhat on the ratio of the grid spacing h to the support size a, but remain practically unchanged in the range $\frac{1}{2}\, a \le h \le 2\, a$.
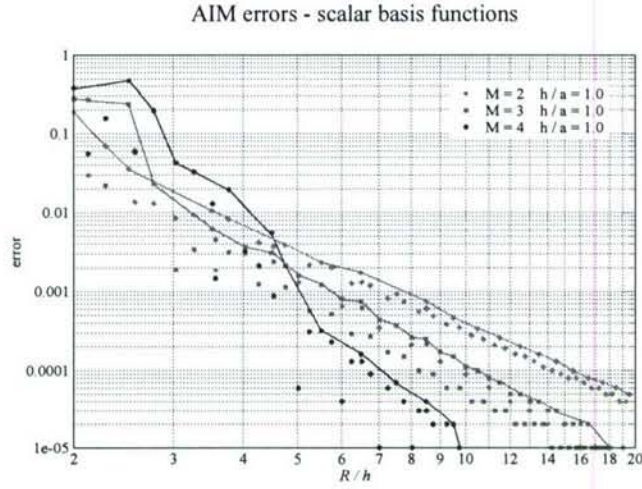
44

AIM errors - scalar basis functions

Figure 19: Relative errors of the AIM approximation to matrix elements for scalar basis functions, for expansion orders $M = 2, 3, 4$, plotted as functions of the distance R between the cell centers. The lines indicate approximate "envelopes" of maximum errors.

The Table 4 summarizes results of the error analysis in terms of the required near-field range as a function of the expansion orders M and the desired accuracy in the matrix elements, from 1.0 % to 0.2 %. The parameter d in the Table (defining the near-field range in AIM through Eq.(D.20)) were determined on the basis of numerically computed errors, such as shown in Fig. 19.

Table 4: AIM near field range d as a function of the expansion order M and error tolerance

M	AIM: d		
	scalar basis functions		
	1.0%	0.5%	0.2%
2	2	3	4
3	1	1	2
4	0	1	1

45

D.5 Near- and far-field computation in AIM

We present here the main elements of the implementation of the AIM algorithm for matrix-vector multiplication; they will be used in the following to obtain the computational complexity of the algorithm.

In the compressed matrix representation (D.6) the near-field part of the matrix (D.7) is the conventional MoM matrix restricted to the near-field range and stored in a sparse form. Matrix-vector multiplication involving this matrix is implemented in straightforward way as a sparse-matrix-vector product.

Eq.(D.8) implies that the far-field part of the matrix-vector product is

$$y_\alpha^{\text{Far}} = \sum_{\beta=1}^{N} \sum_{\mathbf{u},\mathbf{v}\in\mathcal{G}} V_{\alpha\mathbf{u}}\, g(\mathbf{u}-\mathbf{v})\, V_{\beta\mathbf{v}}\, x_\beta \tag{D.22}$$

where the sums are taken over all Cartesian grid nodes (cell centers) $\mathbf{u}$ and $\mathbf{v}$.

Equivalently, the matrix-vector multiplication (D.22) can be executed as the sequence of three steps

$$(A):\quad \widehat{x}_\mathbf{v} = \sum_{\beta=1}^{N} V_{\beta\mathbf{v}}\, x_\beta \qquad \text{for all } \mathbf{v}\in\mathcal{G}\,, \tag{D.23a}$$

$$(B):\quad \widehat{y}_\mathbf{u} = \sum_{\substack{\mathbf{v}\in\mathcal{G}\\ \mathbf{v}\neq\mathbf{u}}} g(\mathbf{u}-\mathbf{v})\, \widehat{x}_\mathbf{v} \qquad \text{for all } \mathbf{u}\in\mathcal{G}\,, \tag{D.23b}$$

$$(C):\quad y_\alpha^{\text{Far}} = \sum_{\mathbf{u}\in\mathcal{G}} V_{\alpha\mathbf{u}}\, \widehat{y}_\mathbf{u} \qquad \text{for all } \alpha=1,2,\ldots,N\,. \tag{D.23c}$$

The convolution over the Cartesian grid nodes in Eq.(D.23b) is implemented by means of an FFT: We compute the FFTs of the Green function expansion coefficients,

$$(B0):\qquad \widetilde{g}(\mathbf{Q}) = \sum_{\mathbf{v}\in\mathcal{G}} \mathcal{F}_{\mathbf{Q}\mathbf{v}}\, g(\mathbf{v}) \qquad \text{for } \mathbf{Q}\in\widetilde{\mathcal{G}}\,, \tag{D.24a}$$

of the input Cartesian vector x,

$$(B1):\qquad \widetilde{x}_\mathbf{Q} = \sum_{\mathbf{v}\in\mathcal{G}} \mathcal{F}_{\mathbf{Q}\mathbf{v}}\, \widehat{x}_\mathbf{v} \qquad \text{for } \mathbf{Q}\in\widetilde{\mathcal{G}}\,, \tag{D.24b}$$

(where the matrix $\mathcal{F}$ represents the discrete Fourier transform, and $\widetilde{\mathcal{G}}$ is the conjugate Cartesian grid), we evaluate the product of the Fourier transforms,

$$(B2):\qquad \widetilde{y}_{\mathbf{Q}} = \widetilde{g}(\mathbf{Q})\,\widetilde{x}_{\mathbf{Q}} \qquad\qquad \text{for } \mathbf{Q} \in \widetilde{\mathcal{G}}\,, \qquad (D.24c)$$

and take the inverse Fourier transform of the product,

$$(B3):\qquad \widehat{y}_{\mathbf{u}} = \sum_{\mathbf{Q}\in\widetilde{\mathcal{G}}} \mathcal{F}^{-1}_{\mathbf{uQ}}\,\widetilde{y}_{\mathbf{Q}} \qquad\qquad \text{for } \mathbf{u} \in \mathcal{G}\,. \qquad (D.24d)$$

Of course, the FFT of the Green function in step (B0) has to be computed and stored only once.

D.6   Computational complexity in AIM

The computational complexity estimates we give here are obtained for a volumetric problem, with the simple geometry and Cartesian grid as specified before in Section D.3.

Near-field computation. According to Eq.(D.20), the AIM near-field volume of a given basis function is a cube of side length $2\,(d+M)\,h$, containing on the average n_C (Eq.(D.18)) unknowns. It follows that the total number of near-field matrix elements is

$$\mathcal{N}[A^{\text{Near}}]_{\text{AIM}} = \tfrac{1}{2}\,N\,[2\,(d+M)]^3\,n_C = 4\,(d+M)^3\,\frac{N^2}{N_{\mathcal{G}}}\,, \qquad (D.25)$$

with the factor $\tfrac{1}{2}$ due to the symmetry of the matrix. Consequently, the near-field computation requires

$$\text{Nop[near]}_{\text{AIM}} = 8\,(d+M)^3\,\frac{N^2}{N_{\mathcal{G}}} \qquad (D.26)$$

operations (complex multiplications and additions).

Far-field computation. Conversion of the set of MoM unknowns to the Cartesian vector in step (A) (Eq.(D.23a)) involves $(M+1)^3$ grid points in an expansion cube for each unknown; the same applies to the inverse operation (C) of Eq.(D.23c). The number of complex multiplication and additions is thus

$$\text{Nop[step A]}_{\text{AIM}} = \text{Nop[step C]}_{\text{AIM}} = 2\,(M+1)^3\,N\,. \qquad (D.27)$$

In the FFT-based implementation of step (B), i.e., steps (B1) – (B3) of Eqs. (D.24), the numbers of operations are

$$\begin{aligned}\text{Nop[step B1]}_{\text{AIM}} = \text{Nop[step B3]}_{\text{AIM}} &= \tfrac{5}{2}\,8N_{\mathcal{G}}\,\log_2(8N_{\mathcal{G}})\\ &= 20\,N_{\mathcal{G}}\,\log_2(8N_{\mathcal{G}})\,,\end{aligned} \qquad (D.28)$$

47

where the factor 8 comes from the zero padding of the Cartesian vectors, and where we assumed the FFT complexity as for the radix-2 algorithm, i.e., $\frac{5}{2}n\log_2 n$ for a vector of length n. Step (B0), which has to be carried out only once, belongs to the compressed matrix set-up, and we don't count it as a part of matrix-vector multiplication.

Finally, step (B2) of Eq.(D.24c) – multiplication of Cartesian vectors – requires

$$\text{Nop[step B2]}_{\text{AIM}} = 16\,N_{\mathcal{G}} \tag{D.29}$$

operations. The total numbers of operations in the far-field computation (steps (A), (B), and (C)) is thus

$$\text{Nop[far]}_{\text{AIM}} = 4\,(M+1)^3\,N + 8\,[2 + 5\,\log_2(8N_{\mathcal{G}})]\,N_{\mathcal{G}} \,. \tag{D.30}$$

Total computational cost. By collecting contributions of Eqs. (D.26) and Eqs. (D.30) we find the total computational complexity of matrix-vector multiplication in AIM,

$$\text{Nop[}A\,x\text{]}_{\text{AIM}} = 8\,(d+M)^3\,\frac{N^2}{N_{\mathcal{G}}} + 4\,(M+1)^3\,N + 8\,[2 + 5\,\log_2(8N_{\mathcal{G}})]\,N_{\mathcal{G}} \tag{D.31}$$

Thus, if we define

$$\xi \equiv \frac{N_{\mathcal{G}}}{N} \,, \tag{D.32}$$

the computational cost per unknown is

$$\frac{1}{N}\,\text{Nop[}A\,x\text{]}_{\text{AIM}} = \frac{a_1(d,M)}{\xi} + a_2(M) + [a_3 + a_4\,\ln(\xi\,N)]\,\xi \tag{D.33}$$

with

$$a_1(d,M) = 8\,(d+M)^3 \,, \tag{D.34a}$$
$$a_2(M) = 4\,(M+1)^3 \,, \tag{D.34b}$$
$$a_3 = 136 \,, \tag{D.34c}$$
$$a_4 = \frac{40}{\ln 2} \simeq 57.7 \,. \tag{D.34d}$$

We list in Table 5 the values of the coefficients for several choices of the near-field ranges and expansion orders, based on the error estimates summarized in Table 4. We have selected the parameters (d, M) corresponding to the expected 1% error level, as given in Table 4. In the case of AIM we chose the parameters for the less favorable case of vector basis functions.

Table 5: Coefficients in matrix-vector multiplication algorithm complexity in AIM

		AIM			
d	M	$a_1(d, M)$	$a_2(M)$	a_3	a_4
10	2	13,824	108	136	57.7
3	3	5,532	256	136	57.7

D.7 Storage in AIM

Storage (in complex numbers) required for the compressed matrix representation in the AIM algorithm is obtained in close analogy to the complexity estimates:

$$\text{Mem}[A^{\text{Near}} + A^{\text{Far}}]_{\text{AIM}} = 4 \, (d + M)^3 \, \frac{N^2}{N_{\mathcal{G}}} + (M + 1)^3 \, N + 8 \, N_{\mathcal{G}} \, , \quad \text{(D.35)}$$

i.e., in terms of the ratio ξ (Eq.(D.32)) the total storage per unknown is

$$\frac{1}{N} \, \text{Mem}[A]_{\text{AIM}} = \frac{\widehat{a}_1(M)}{\xi} + \widehat{a}_2(M) + \widehat{a}_3 \, \xi \quad \text{(D.36)}$$

with

$$\widehat{a}_1(d, M) = 4 \, (d + M)^3 \, , \quad \text{(D.37a)}$$
$$\widehat{a}_2(M) = (M + 1)^3 \, , \quad \text{(D.37b)}$$
$$\widehat{a}_3 = 8 \, . \quad \text{(D.37c)}$$

The values of the coefficients $\widehat{a}_i$ for typical parameters d and M are given in the Table 6.

Table 6: Coefficients in relative matrix-vector matrix storage in AIM

		AIM		
d	M	$\widehat{a}_1(d, M)$	$\widehat{a}_2(M)$	$\widehat{a}_3$
10	2	6,912	27	8
3	3	2,766	64	8

D.8   Optimization of parameters in AIM

In Figs. 20 and 21 we plot the computational costs and memory requirements (per unknown) for the AIM algorithm in a rather wide range of the parameter $\xi = N_\mathcal{G}/N$, covering typical values encountered both in volume and in surface problems.
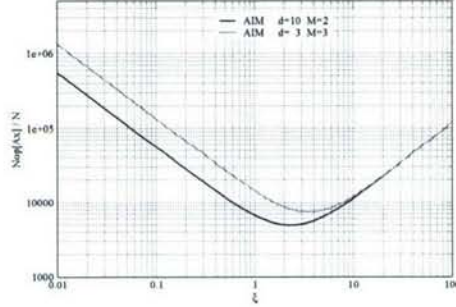

Figure 20: The matrix-vector multiplication cost-per-unknown in the AIM algorithm for $N = 10^6$, plotted as a function of $\xi = N_\mathcal{G}/N$, in the doubly-logarithmic scale.
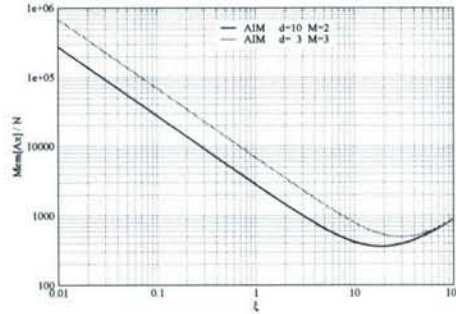

Figure 21: The matrix storage per unknown in the AIM algorithm, plotted as a function of $\xi = N_\mathcal{G}/N$, in the doubly-logarithmic scale.

Figs. 20 and 21 show that the minimum cost of the matrix-vector multiplication (which we take as the decisive factor in the optimization) is

50

achieved at $\xi \equiv N_G/N \simeq 2$. According to the discussion of Section D.3, the grid spacing corresponding to this value of ξ is

$$h \simeq a\,(c_V\,\xi)^{-1/3} \simeq 0.46\,a \;, \tag{D.38}$$

where a is the spatial resolution of the MoM discretization. Clearly, this value should not be taken too literally, since the actual number of MoM unknowns may strongly depend on the geometry; nevertheless, Eq.(D.38) indicates that the *optimal grid spacing is close to* (and likely smaller than) the resolution of the geometry discretization.

Fig. 21 indicates that the minimum storage is attained for a higher value of ξ, $\xi \simeq 20$, corresponding to the grid spacing smaller by another factor $10^{-1/3} \simeq 0.46$. The estimated storage at $\xi = 2$ is exceeds its minimum value by about a factor 4. Therefore, if memory reduction is of higher priority, the grid spacing may be decreased accordingly to reach the overall optimum.

We also see from Fig. 20 that the *quadrupole expansion* (order $M = 2$) yields the cost almost a factor of 2 lower than the next order ($M = 3$) expansion. At the same time, Fig. 19 shows that, for acoustics, the *near-field range of 3 to 4 grid spacings* is sufficient to reduce the far-field error to the 1% level. Further empirical analysis has shown that *the optimal compression parameters*, ensuring errors not larger than 1 %, are

$$h \simeq \tfrac{1}{2}a \;, \qquad R^{\mathrm{AIM}}_{\mathrm{min}} \simeq 3\,h \;, \qquad M = 2 \tag{D.39}$$

(cf. Eq.(D.20)). This conclusion applies to problems with moderately to highly subwavelength discretization, i.e., with tetrahedron size

$$a \lesssim \frac{\lambda}{20} \;, \tag{D.40}$$

i.e., in practice, to all problems we are considering here; it has been confirmed by many practical computations for large problems (up to several million unknowns) which we report on in Section 3.4.

51

References

[1] R. Coifman, V. Rokhlin, and S. Wandzura, "The Fast Multipole Method for the wave equation: a pedestrian prescription," *IEEE Antennas and Propagation Magazine*, vol. 35, pp. 7–12, 1993.

[2] E. Bleszynski, M. Bleszynski, and T. Jaroszewicz, "AIM: Adaptive integral method for solving large-scale electromagnetic scattering and radiation problems," *Radio Science*, vol. 31, pp. 1225–1251, 1996.

[3] P. M. Morse and K. U. Ingard, *Theoretical Acoustics*. New York: McGraw-Hill, 1968.

[4] E. Bleszynski, M. Bleszynski, and T. Jaroszewicz, "Least-squares based far-field expansion in the Adaptive Integral Method (AIM)," in *Proceedings of the 13th Annual Review of Progress in Applied Computational Electromagnetics*, Monterey, CA, March 17-21 1997, pp. 944–950.

[5] W. Goldsmith and K. L. Monson, "The state of head injury mechanics: past, present, and future. Part 2: Physical experimentation," *Critical Reviews in Biomedical Engineering*, vol. 2, pp. 105–207, 2005.

[6] S. K. Kyriacou, A. Mohamed, K. Miller, and S. Neff, "Brain mechanics for neurosurgery; modeling issues," *Biomechanics and Modeling in Mechanobiology*, vol. 1, pp. 151–164, 2002.

[7] J. H. McElhaney, J. L. Fogle, J. W. Melvin, R. R. Haynes, V. L. Roberts, and N. M. Alem, "Mechanical properties of cranial bone," *J. Biomech.*, vol. 3, pp. 495–511, 1970.

[8] L. Z. Schuck and S. H. Advani, "Rheological response of human brain tissue in shear," *Trans. ASME J. Basic Eng.*, pp. 905–911, 1972.

[9] R. Hickling and M. L. Wenner, "Mathematical model of a head subjected to an axisymmetric impact," *J. Biomech.*, vol. 6, pp. 115–132, 1973.

[10] C. Ljung, "A model for brain deformation due to rotation of the skull," *J. Biomech.*, vol. 8, pp. 263–274, 1975.

[11] B. Donnely and J. Medige, "Shear properties of human brain tissue," *J. Biomech. Eng.*, vol. 119, pp. 423–432, 1997.

[12] B. Håkansson, A. Brandt, P. Carlsson, and A. Tjellström, "Resonance frequencies of the humen skull *in vivo*," *J. Acoust. Soc. Am.*, vol. 95, pp. 1474–1481, 1994.

[13] B. Håkansson and S. Stenfelt, "Vibration characteristics of bone conducted sound *in vitro*," *J. Acoust. Soc. Am.*, vol. 107, pp. 422–431, 2000.

[14] D. Colton and R. Kress, *Integral equation methods in scattering theory.* John Wiley & Sons, 1983.